POLITECNICO DI TORINO
Repository ISTITUZIONALE

A Method to Compute the Ultimate Displacements in Reinforced Earth Rockfall Protection Embankments: A Perspective for the Design

Original
A Method to Compute the Ultimate Displacements in Reinforced Earth Rockfall Protection Embankments: A Perspective for the Design / Vigna, S., Marchelli, M., De Biagi, V., Di Pietra, V., Saltarin, S., Peila, D.. - In: ROCK MECHANICS AND ROCK ENGINEERING. - ISSN 0723-2632. - (In corso di stampa). [10.1007/s00603-025-04801-4]

Availability:
This version is available at: 11583/3002395 since: 2025-08-12T11:18:13Z

Publisher:
Springer

Published
DOI:10.1007/s00603-025-04801-4

Terms of use:

This article is made available under terms and conditions as specified in the corresponding bibliographic description in the repository

Publisher copyright

(Article begins on next page)

17 November 2026

Rock Mechanics and Rock Engineering
https://doi.org/10.1007/s00603-025-04801-4

ORIGINAL PAPER

A Method to Compute the Ultimate Displacements in Reinforced Earth Rockfall Protection Embankments: A Perspective for the Design

Stefano Vigna[1] · Maddalena Marchelli[1] · Valerio De Biagi[2] · Vincenzo Di Pietra[1] · Simone Saltarin[1] · Daniele Peila[1]

Received: 6 December 2024 / Accepted: 17 July 2025
© The Author(s) 2025

Abstract

Rockfall protective embankments (RPEs) offer a cost-effective solution for mitigating rockfall hazards, particularly in scenarios involving high-energy or repeated impacts. Among the available technologies, reinforced earth embankments are widely adopted, although their design methodologies remain a subject of ongoing research. This study investigates the behavior of a reinforced earth RPE, with a focus on characterizing the evolution of the displacement field up to collapse induced by a localized punching force, representing the impact of a falling block, applied to one face of the structure. Two reinforcement configurations are examined: unidirectional geogrid and double-twist steel mesh with metallic clips. Given the scarcity of full-scale experimental data and the practical challenges associated with such tests, a series of reduced-scale tests was designed and conducted. Geometric and mechanical similitude was ensured through the application of the Buckingham Π-theorem. The tests were performed under quasi-static conditions to isolate the displacement field associated with soil layer sliding, neglecting inertial effects. Throughout the tests, both force and displacement histories were continuously recorded and analyzed. The results provide valuable insights into the volume of embankment affected by impact and the pre-collapse displacement patterns for both reinforcement types. Two extended finite element method (XFEM) models were developed to simulate the behavior of each reinforcement configuration. Model calibration was enhanced using photogrammetric reconstruction of the embankment's downslope face, with point cloud data collected throughout the testing phase, enabling accurate validation of simulated deformation patterns. Finally, a full-scale dynamic impact test from the literature was used to calibrate a real-scale numerical model and to assess the consistency between dynamic and quasi-static responses of the same embankment system.

Highlights

- Reduce-scale tests of rockfall reinforced embankments to evaluate the collapse.
- The energy dissipation due to friction is determined from quasi-static tests.
- A photogrammetric network defines the 3D displacement field during the test.
- The tests serve to calibrate the numerical models to define pre-collapse conditions.
- Comparison with real-scale tests is done to check the quality of the predictions

✉ Stefano Vigna
stefano.vigna@polito.it

Maddalena Marchelli
maddalena.marchelli@polito.it

Valerio De Biagi
valerio.debiagi@polito.it

Vincenzo Di Pietra
vincenzo.dipietra@polito.it

Simone Saltarin
simone.saltarin@polito.it

Daniele Peila
daniele.peila@polito.it

[1] Department of Environment, Land and Infrastructure Engineering, Politecnico di Torino, Corso Duca degli Abruzzi, 24, 10129 Torino, Italy

[2] Department of Structural, Geotechnical and Building Engineering, Politecnico di Torino, Corso Duca degli Abruzzi, 24, 10129 Torino, Italy

Published online: 12 August 2025

Keywords Rockfall protection embankment · Pseudo-static test · Reduced-scale test · Numerical model · Failure analysis · Pre-collapse dispalcements

1 Introduction

Rockfall phenomena represent a significant hazard in mountain environment, with possible harmful consequences for people, structures, and infrastructures (Ferlisi et al. 2012; Marchelli et al. 2022a). Rockfall protection embankments (RPEs) represent valuable passive mitigation measures, widely adopted especially in such cases involving the presence of multiple impacting blocks, very high kinetic energies or large blocks, and where the slope toe is almost flat (Lambert and Bourrier 2013; Grimod and Giacchetti 2013; Hofmann and Vollmert 2020). RPEs are defined by Lambert and Kister (2017) as any structure in elevation of at least 2 m with respect to the ground, mostly made of granular materials built with the aim of intercepting falling blocks whatever the cross-sectional shape of the embankment.

The RPEs are built directly on site and, due to their massive structure, if correctly designed, they can withstand impacts up to 50 MJ (Lambert and Bourrier 2013; Volkwein and Gerber 2011; Marchelli et al. 2022b). In the last decades, several technologies of RPEs have been developed, differing for the adopted materials, their assembly, and the cross-sectional shape. A comprehensive classification is presented in Peila et al. (2011) and Lambert and Kister (2017, 2018a).

The present study focuses on the behavior of reinforced earth RPEs, named in the following as RE-RPEs, which is a widely adopted technology (Korini et al. 2021). It consists of an overlap of *n* layers of compacted soil, typically of cohesionless material (generally recovered on site), each wrapped in a tensile resistant element, defining a trapezoidal cross-sectional shape (Fig. 1). It should be noted that in the sketch, both faces present reinforced earth, while this is not always the case. RE-RPEs have several advantages compared to other types of protection embankments, say natural earth embankments: with a lower footprint of the embankment for equal design energy (Blovsky 2002b), the resisting capabilities of the formers against high or high-energy impacts can be easily obtained increasing both the height or the base (Wyllie 2014). This results in a reduced maintenance and environmental impact (Rimoldi and Brusa 2024). The tensile resistant element, hereafter named as *reinforcement*, usually consists of either HDPE (high-density polyethylene) geogrids, or double-twist (DT) wire mesh. The

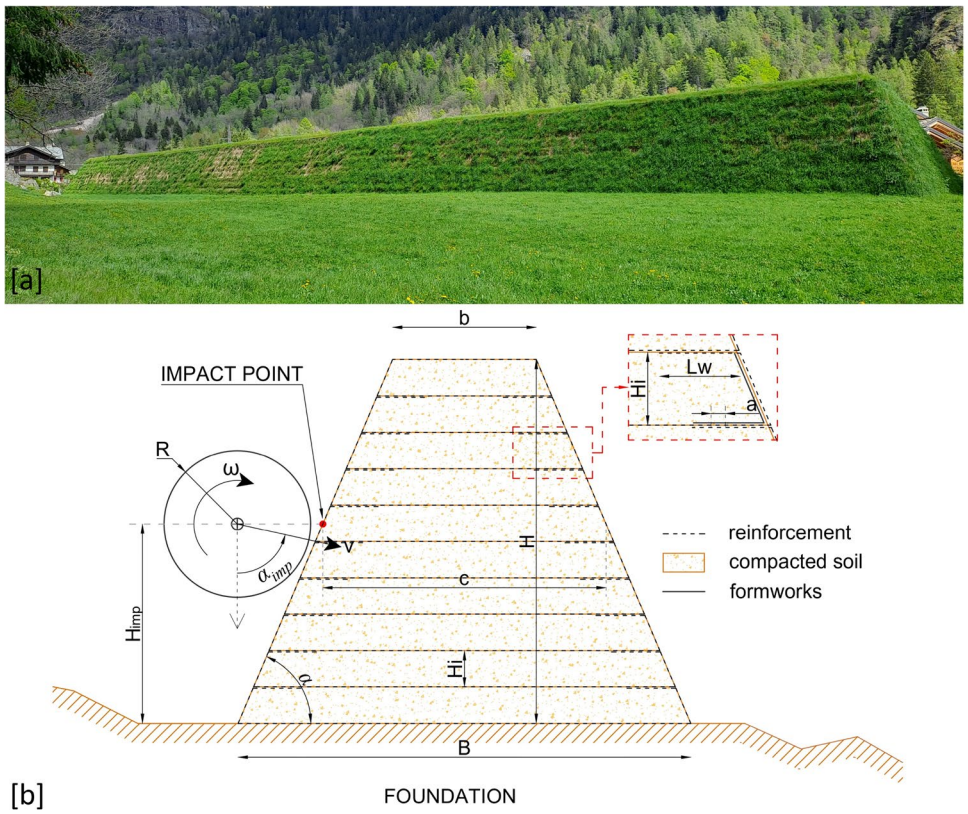


Fig. 1 **a** RE-RPE reinforced with Terramesh system located in Aosta Valley (IT). **b** Cross-section and nomenclature used in the paper

present study focuses on RE-RPEs reinforced with these two reinforcement systems, which are detailed in Sect. 1.1.

Currently, the structural response of impacted RE-RPEs has not been comprehensively investigated due to the limited number of available data on real-scale impact tests (Peila et al. 2007; Clerici et al. 2013; Mongiovi et al. 2014; Korini et al. 2021). Peila et al. (2007) tested RE-RPEs with HDPE geogrids at an impact energy of 4200 kJ. As highlighted in the literature (Peila et al. 2000, 2002; Carotti et al. 2004; Peila et al. 2007, 2011; Ronco 2010), the energy dissipating mechanisms are mainly identified in: (i) plastic strains for soil compaction of the impacted face resulting in irreversible displacements, and (ii) sliding friction at the geogrids' interfaces of the impact-disturbed volume of RE-RPE. The volume disturbed by the impact, called *impact-disturbed zone* (IDZ) in literature (Kister 2015), has the shape of a truncated prism which height involves all the impacted layers, while the lateral influence is geometrically bounded: approximately equal to the width of the block in the upslope face, opening downslope with an angle of approximately $\psi = 45°$. Recently, Rimoldi and Brusa (2024), in line with the findings by Blovsky (2002a), have suggested different values of ψ in function of the technology and the impact conditions. Similar experimental results about the energy dissipating mechanisms have been obtained by Mongiovi et al. (2014). Other tests on RE-RPEs reinforced with geogrids have been carried out by Clerici et al. (2013) and Korini et al. (2021). Lambert et al. (2020) performed full-scale tests on slender vertical-sided gabion structures designed to resist rockfall impacts. From a numerical point of view, several finite element (FE) and discrete element (DE) models of rockfall protection embankments have been defined (Bertrand et al. 2007; Breugnot et al. 2016; Plassiard and Donzé 2009, 2010; Kanno et al. 2021; Vigna et al. 2023). It is worth noting that a few of these refers to reinforced earth technology (Carotti et al. 2000; Oggeri et al. 2021). The back-analyses of the tests done by Peila et al. (2007), Ronco et al. (2009), and Ronco (2010) allowed to determine the energy contributions to stop the block in the specific simulated case: 80%–85% of the kinetic energy is dissipated in soil plasticity (E_p), 5–10% in friction (E_f). The remaining 0–5% is represented by recoverable strain energy (E_s). Such energy dissipating mechanisms have been confirmed by Lu et al. (2021) and Di Prisco and Vecchiotti (2003). In general, inertia effects are inherently accounted for in the plastic energy dissipation term when using explicit dynamic solvers such as Abaqus/Explicit. In these simulations, the total internal energy is typically decomposed into elastic, plastic, and other dissipative components. However, due to the dynamic nature of the analysis, inertia, through mass and acceleration, affects the evolution of stress and strain, thereby indirectly contributing to plastic work and its associated energy dissipation. The plastic energy term, thus, includes irreversible deformation, which is influenced by the dynamic loading history, including inertial effects. (Cimellaro and Marasco 2018).

Inertia plays a key role in the penetration resistance of the embankment. Under dynamic loading, inertia increases the buttress effect associated with the embankment volume opposite the impacted face (along the horizontal direction) Lambert and Bourrier (2013). This observation at the macroscale also holds at the microscale: the amplitude of the stress at a given point and the propagation of the compression wave depend of the inertia of the system body in the direction towards which the compressive wave travels.

Several analytical approaches for the design of the RE-RPEs have been proposed (Carotti et al. 2004; Jaecklin 2006; Brunet et al. 2009; Wyllie 2014; Bragonzi et al. 2016; Lambert and Kister 2018b; Marchelli et al. 2022b; Rimoldi and Brusa 2024). The outputs of the numerical back-analyses form the bases of the "energy-based approach", first introduced by Peila et al. (2007) and further investigated by Lambert and Bourrier (2013). This method enables the determination of the maximum upslope and downslope displacements $\delta_{u,max}$ and $\delta_{d,max}$, i.e., those after an impact occurs, which are fundamental to assess the structure stability. The downslope displacement is essentially due to the sliding of the impact-disturbed zone, while the upslope displacement also includes the penetration of the block which forms a crater. Recently, Marchelli et al. (2022b) have proposed an enhancement to the method, which provides an insight into the percentages of energy dissipated by friction and by plastic deformation. This analytical method shows how the ranges of energy dissipation found in the beforementioned tests of Peila et al. can be considered valid for several common applications. Other simplified methods currently in use include the "pseudo-static method" which neglects the dynamic nature of the impact by considering an equivalent static force. The Austrian standard ONR 24810 (ONR 24810 2021) is a prominent example of this approach. Lastly, the "penetration method" employs formulas derived from other engineering fields (e.g., ballistics, tamping) to compute $\delta_{u,max}$. Notable examples include formulations proposed by Kar (1978), Li and Chen (2003), Calvetti and Di Prisco (2007), Wang and Cavers (2008), and Grimod and Giacchetti (2013). However, Lambert and Kister (2017) have shown that this formula tends to give a large dispersion of the outputs. However, to the knowledge of the authors, no deep study on the behavior of RE-RPEs with DT with focus on the effects provided by the clips has been conducted so far. As suggested by Lambert and Kister (2017), energy-based approaches are very profitable, even though they required the knowledge of dissipative mechanisms, displacements and volume disturbed by the impact. It should be noted that, although it is possible to compute $\delta_{u,max}$ and $\delta_{d,max}$ after an impact through analytical or numerical methods, these values have been, so far, compared with

the limit displacements, defined from geometrical considerations, such as, the length of the wrap, or the position of the centers of mass of the layers. To the knowledge of the authors, the values that correspond to the instant before the collapse (pre-collapse condition), $\delta_{u,all}$ and $\delta_{d,all}$, have not been defined, yet. The knowledge of these pre-collapse values, depending on the applied reinforcement technology, especially for the downslope displacements, is essential in the design step as they represent the threshold values that provide the capacity of the protection system. At present, this information can be obtained through a fully dynamic numerical analysis in which the interactions between (i) the block and the RE-RPE, and (ii) within the various layers of the embankment must be correctly modeled. This latter approach requires a strong expertise and needs reliable data from real-scale impact tests. For these reasons, it cannot be considered feasible in the design phase of the rockfall risk mitigation structure.

As a futher problem, the maintenance of existing RE-RPEs has not yet been addressed: if an RE-RPE has been impacted, it is crucial for local administrations to know how much displacement the structure can still withstand, thereby understanding the residual risk.

The scope of the present paper is to determine the downslope displacements that can be associated to the pre-collapse condition of RE-RPEs realized with two different reinforcement types. As an hypothesis, as further detailed, the sliding between the various parts is considered as the energy dissipating mechanism that affects the downslope displacements. For this reason, reduced-scale tests on both technologies, were conceived and realized by the authors. As the reinforcements modify the way the various parts slide, the attention is specifically oriented towards the frictional resisting mechanism. During the tests, the two RE-RPEs were driven to failure mimicking, in quasi-static conditions, the displacement field due to soil-layer sliding caused by an impact, allowing for step-by-step observation of the resistant frictional mechanisms. The adoption of quasi-static tests does not obviously take into account the inertia contribution. This results in a lower penetration resistance compared to dynamic loading and thus to lower stresses in the embankment (and consequently in less soil plasticization) in the upslope face. The tests were continuously monitored by a photogrammetric network, which, thanks to innovative post-processing, enabled the reconstruction of the downslope deformations throughout the tests. All these aspects are detailed in Sect. 2. The tests were used to calibrate a FEM numerical model, developed with Abaqus/Explicit (Sect. 3.3). The whole history of the deformation recorded during the tests was used as benchmark for the numerical model, not limiting, thus, the back-analysis to single values, only. The experiments and the numerical simulations served to investigate the resisting frictional mechanisms for both reinforcement technologies and the force–displacement curves obtained in quasi-static test condition were analyzed to define the pre-collapse values in the numerical model. The suitability of this curve for the design also in dynamic conditions, limiting thus the need of complex dynamic numerical model for the design, was finally verified numerically simulating the embankment tested by Peila et al. (2007) and comparing results in quasi-static and impact conditions (Sect. 4). Finally, conclusions and future perspective are outlined (Sect. 5).

1.1 Detail About the Reinforcement Systems

As mentioned, two different technologies for the reinforcement were considered. The first system consists of a double twist mesh with galvanized steel wire coated from a polymac protection layer (2.20/3.20 mm). This is commercially available from Officine Maccaferri produces as the Terramesh system (Officine Maccaferri Italia 2022). The second reinforcement system is a light unidirectional HDPE geogrid, commonly used in the construction of RE-RPEs. Such product is available from Reinforcement Earth/Terre Armée, Tenax (TT045), or Officine Maccaferri (Paragrid 40/5). Both technologies require the reinforcement layers to be wrapped around a trapezoidal volume of compacted soil, providing a flap of length L_W between the adjacent layers above and below (Fig. 1b). The reinforcement in both technologies is installed in such a way that the direction offering larger stiffness (bearing capacity of the reinforcement) is transversal to the embankment.

The formworks adopted to achieve the desired slope angle of the side banks (α) and the height of each layer (H_i) are typically made of electro-welded steel mesh. For geogrids, L-shaped formworks with a width of 3–4 m are used. The geogrid layers are placed inside the formworks along with a geotextile layer to retain fine materials, and then filled with compacted soil. Each geogrid panel overlaps slightly with the adjacent panel.

In RE-RPEs with the Terramesh system, 3-m-wide precast elements are assembled at the factory by placing the DT reinforcement onto rectangular formworks and connecting them with metal clips. The formworks are then fitted with ties and brackets to maintain the slope inclination α. Onsite, these elements are connected along the boundaries of each panel during embankment construction using metal clips. The clips are installed with a defined spacing (a) and characterized by a maximum tensile strength (T_{max}), as determined in accordance with the procedures outlined in EAD 200086-00-0602 (2019). The schematic of the Terramesh system is shown in Fig. 2.

From here on, the terms “System A” and “System B” are used in reference to the models to highlight the absence

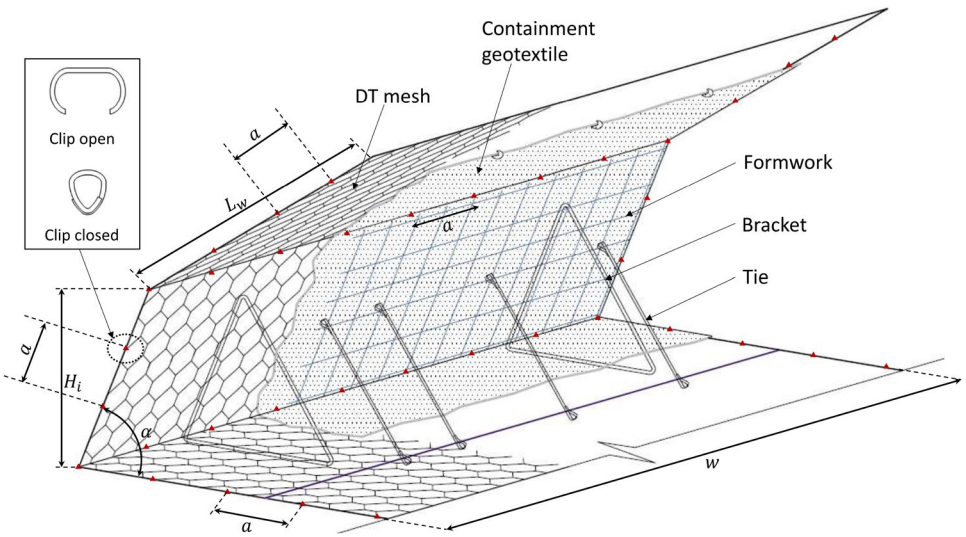


Fig. 2 Scheme of the Terramesh system by Maccaferri: 3-m-wide prefabricated element positioned on site and jointed laterally, above and below with clips to other identical elements. (Modified from Officine Maccaferri Italia (2022) data-sheet)

(geogrid technoloy) or the presence (Terramesh system) of the clips, respectively.

2 Methodology

An experimental campaign devoted to the study of the energy dissipating mechanisms that arise in both the technologies adopted in the construction of RE-RPEs was conceived and carried on. To limit costs and technical difficulties, in situ reduced-scale experiments were developed, scaling the geometry and the mechanical properties according to Buckingham Π-theorem, as detailed in Sect. 2.1. To clearly identify the number and the resisting contributions of the involved layers, a quasi-static load condition was imposed, applying a force at mid-height of the embankments thanks to a hydraulic jack, pushing a punch made with a steel circular plate. Considering a quasi-static load case, instead of a dynamic impact, implies that the inertial resisting contribution is neglected. This condition allows to study the upslope and downslope displacements fields caused by a block in a controlled manner to determine the pre-collapse $\delta_{d,all}$ value.

The adopted methodology is summarized below, and detailed in the following sections:

1. Conceptualization of reduced-scale tests with an appropriate scaling law and suitable materials to comply with the geometrical and mechanical similitude.
2. Conceptualization of the monitoring system and techniques.
3. Construction of the scaled RE-RPEs, with both technologies and execution of the test.
4. Analysis of the force–displacement history and energy dissipating mechanisms.
5. Development of numerical FEM models, back-analyzing the performed experiments.
6. Modeling of a real-scale embankment and comparison with existing real-scale test.

2.1 Reduced-Scale Model for the Tests

Reduced-scale tests have often been used in literature and in different fields of engineering to study problems difficult to replicate at the real scale (Jones 2011; Ambur et al. 2005; Coutinho et al. 2016; Oshiro and Alves 2004), with particular reference to impact issues (Alves and Oshiro 2006). Referring to RPE, small-scale laboratory tests were conducted by Blovsky (2002a, 2002b), Hoffmann and Mölk (Hofmann et al. 2013, 2017), Kister and colleagues (Kister et al. 2017; Lambert and Kister 2017), and Lu et al. (2021), scaling the geometry by 1/50, 1/33, 1/9, and 1/4, respectively. All these studies have not involved reinforced earth embankments adopting DT and clips.

In dealing with objects at different scales, the geometrical and mechanical similitude between the bodies can be achieved if specific rules apply. To this aim, Buckingham Π-theorem (Buckingham 1914) was applied to design the reduced-scale test, i.e., the model, and to translate the measured quantities in terms of force and displacement into the physical model of a real-scale embankment, i.e., the prototype (Shehadeh et al. 2015). The theorem is based on the fact that, at any given scale, whether model or prototype, it is possible to define dimensionless quantities, known as Π numbers. These quantities are scale-independent, and therefore retain the same value across all scales. The theorem states that the behavior of the system can be described starting from the dimensionless Π, rather than from the variables. Given a set of variables, each with its own physical dimension, it is possible to construct as many Π numbers as

the number of variables minus the number primary physical dimensions (e.g., length, time, mass) appearing in the variables. The normalization variables are selected from the list according to their physical dimension. In the present study, the physical model of the embankment is characterized by k parameters (listed in the first column of Table 1). Among these, $m = 3$ primary physical dimensions, i.e., mass [M], length [L], and time [t] were identified. The number of primary dimensions is equal to the number of the restrictions, according to which a total of $(k - m)$ Π_i-dimensionless terms are defined to describe the problem in the model through an equation G of $(k - m)$ Π_i terms. The equation G represents the equivalent of the dimensionally homogeneous equation F of k physical variables. The Π_i terms are equal for the prototype (identified in the following with subscript $_P$) of the RE-RPE and the model (identified in the following with subscript $_M$), i.e. $\Pi_{i,P} = \Pi_{i,M}$. Among the k parameters, a number $r = 3$ of repeating parameters, which include all of the primary dimensions, were selected to derive the Π_i terms. Defined the scale factors of each parameter λ_i as the ratio between the values of the parameter in the model and in the prototype, the repeating parameters were selected among those whose λ_i is known. In the present case, the length l, the density ρ, and the gravity g were selected as repeating terms. Considering that $\Pi_i^M = \Pi_i^P$, $\forall i$, the scaling factors λ_i can be expressed from the scaling of the repeating terms. Table 1 reports all the k parameters, the Π_i terms, and the scale factors, defining the scale factor of the length equal to λ. Among those listed in Table 1, the dimensionless parameters that are considered the most relevant to describe the system response are those related to the force F and the displacement δ, as they are used to define the pre-collapse conditions.

Based on the previous selection, the following hypoteses were done in designing the model.

Table 1 Scaling law adopted for the reduced-scale tests

Parameters	Symbol	Π_i	Scaling factor λ_i
Length [m]	l	–	λ
Density [kg/m^3]	ρ	–	1
Gravity [m/s^2]	g	–	1
Force [kgm/s^2]	F	$F\, l^{-3} \rho^{-1} g^{-1}$	λ^3
Displacement [m]	δ	$\delta\, l^{-1}$	λ
Tensile resistance of the reinforcement [kg/s^2]	UTS	$UTS\, l^{-2} \rho^{-1} g^{-1}$	λ^2
Stress [kg/ms^2]	σ	$\sigma\, l^{-1} \rho^{-1} g^{-1}$	λ
Strain [-]	ϵ	ϵ	1
Friction coefficient [-]	μ	μ	1
Time [s]	t	$t\, l^{-0.5} g^{0.5}$	$\lambda^{1/2}$

- The tests were carried on in ordinary gravity conditions as the size of the embankments was not compatible with centrifuge setups. To the knowledge of the authors, the only example of RPE testing in centrifuge has been carried out by Lepert and Corté (1988). Hence, the gravity of the model and the one of the prototype are equal, resulting in a scaling factor equal to one.
- The reinforced earth RE-RPE was done with a soil having the same density of the soil in the prototype, resulting in a scaling factor of the density equal to one (Lu et al. 2021).
- Under static loading conditions, the soil mass above and opposite the impact site undergoes progressive displacements. This results in a decreased penetration resistance when compared to dynamic loading scenarios. Consequently, only the obtained downslope displacements are considered representative of the pre-collapse condition.
- Under static loading conditions, the contribution of the stress wave propagation in the vertical direction observed by Lambert et al. (2020), that would cause an upward acceleration, is neglected.
- Velocity was not considered among the investigated parameters as quasi-static tests were performed on the model to address the research question.
- Considering that an impact in the prototype lasts approximately 500 ms, replicating the corresponding inertial effects in the model requires applying the load within 223 ms. However, in the quasi-static tests that were conducted, the load was applied over a much longer duration. As a result, the contribution of inertia was not accurately simulated. This limitation is not a critical aspect of the experimental campaign, which is focused on investigating the frictional resistance mechanisms within the embankment.
- Considering that the purposes of the model are to investigate the resisting mechanisms involving friction, and not plasticization of the soil, model and prototype require the same friction coefficient, μ, which was obtained by considering the same soil characteristics in term of grains size distribution.
- The anisotropy of the reinforcement was neglected in the model (the reinforcement was considered as isotropic). Based on the loading orientation, the direction offering the larger tensile capacity was taken as primary. Secondary directions were not investigated. As detailed, the reinforcement of the model was installed in such a way that the primary direction is transversal to the embankment. The mechanical properties of the reinforcement in the model were determined through uniaxial tests along the primary direction. This reflects the fact that the secondary capacity and stiffness of the reinforcement (along the longitudinal direction) were neglected.

Both the models aim at simulating a real geometry with $H_i = 0.76$ m, $n = 8$, $\alpha = 67°$, $b = 2$ m and $L_W = 1.25$ m (Fig. 1b). A scale factor $\lambda = 5$ was selected to geometrically and mechanically scale the RE-RPEs. All the parameters were scaled according to the third column of Table 1. Table 2 reports the main geometrical and mechanical variables, along with their value in the prototype and in the model. The actual scaling factors are illustrated too, and compared with the expected values, derived from Table 1 considering $\lambda = 5$. In the current design practice, the useful mechanical properties of the reinforcement are the ultimate strain (ϵ_{max}) and the ultimate tensile strength (UTS, expressed in kN/m) obtained through standardized tests, i.e., ASTM D6637 (2015) and EN ISO 10319 (2015) for the geogrid, and EN 10223-3 (2013) for the DT mesh. This means that the different anisotropic behaviors and material constitutive laws of the different technologies do not affect the energy dissipating mechanisms and contribution inside the embankments but only their failure value. These values, properly scaled, were selected to find a suitable material to reproduce, in the prototype, both geogrid and DT reinforcements, following an approach similar to that adopted by Hofmann and Mölk (2012) and Hofmann et al. (2013, 2017). A TT 045 Uniaxial Geogrid produced by Tenax and the double twist mesh of the Terramesh system produced by Maccaferri (Officine Maccaferri Italia 2022) were considered for the prototype embankment. It has to be noted that the real-scale impact tests by Peila et al. (2007) and Mongiovi et al. Mongiovi et al. (2014) have been done on RPEs reinforced with TT 045 Uniaxial Geogrid.

Both materials (geogrid and DT mesh) have comparable strength parameters: $\varepsilon_{max} \approx 15\%$ and UTS ≈ 45 kN/m. To identify the material to be installed in the model, the force per meter-strain behavior of the reinforcements was analyzed. Based on the standardized tests, both material exhibit an elastic stage that is extremely limited followed by a long hardening phase, from which it results that the curves are almost linear from the origin to the ultimate point (Donzé 2006; Lin et al. 2023; Abu El-Soud and Belal 2018). Hence, a unique material, a polypropilene (PP) mesh with a 15 × 15 mm mesh size and 0.4 mm thickness, with scaled parameters was adopted in the prototype, independently from the type of reinforcement. Ten tensile tests were conducted to assess its tensile behavior. The samples were clamped within a testing frame (Fig. 3a) and displacement-controlled tests were performed at 10 mm/min. During testing, a load cell recorded the tensile force while an LVDT measured the vertical displacement field. These tests yielded average values of UTS = 1.278 kN/m and $\varepsilon_{\max} = 0.171$ (Fig. 3b). It is worth noting that the force-per-meter-strain curve of the tested 15 x 15 mm polypropylene mesh is almost linear from the origin to the ultimate point. The mesh is installed in the model in such a way that the testing direction is transversal to the embankment.

As described, clips are used in the DT-reinforcement setup. Specifically, in the Terramesh system, the recommended clips have a tensile capacity of $F_{\max} = 2$ kN and a spacing of $a = 0.2$ m. To simulate these clips, an open ring made from S235 steel wire with a diameter of 0.6 mm was fabricated and tested using the same methodology as the PP mesh, obtaining a value of $F_{\max} \approx 22$ N.

Figure 2 reports the formworks employed in the Terramesh system, to be placed on the side banks and the desired inclination is achieved using two brackets. In contrast, the geogrid system employs L-shaped formworks in cross-section to ensure the proper slope angles. In both technologies, the real-scale formworks are made of a B450C steel with a mesh size of 15 × 15 cm and a diameter of 8 mm, providing a yield tensile force in cross-section of 226.2 kN/m. This parameter was considered for scaling, where the formworks were replaced with a square mesh made of a mild steel mesh having a mesh size of 13 × 13 mm and a diameter of 0.55 mm, resulting in a yield tensile force in cross-section of approximately 8.0 kN/m.

Table 2 Summary of the relevant values of the geometrical and material properties in the prototype and in the model. The values of the actual and expected scaling factors are reported

Component or property	Value in the prototype	Value in the model	Actual scaling factor	Expected scaling factor
RE-RPE base width	716 cm	142 cm	5.08	5
RE-RPE height	608 cm	120 cm	5.06	5
Layer thickness	76 cm	15 cm	5.06	5
Crest width	200 cm	40 cm	5.0	5
Flap length	120 cm	25 cm	5.0	5
Reinforcement strength capacity	45 kN/m	1.278 kN/m	5.93^2	5^2
Reinforcement strain at failure	0.15	0.171	0.88	1
Clips capacity	2 kN	22 N	4.50^3	5^3
Formworks yield force	226.2 kN/m	8.0 kN/m	5.31^2	5^2

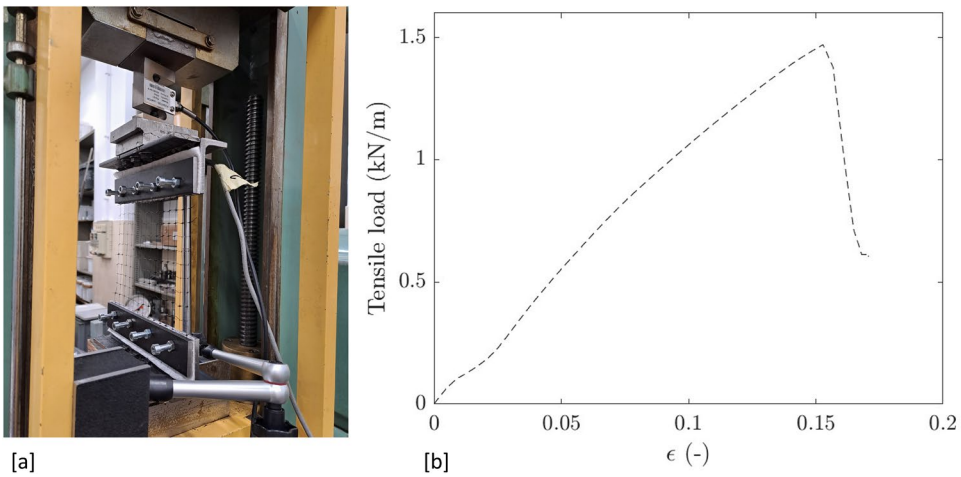


Fig. 3 **a** Set-up of the tensile tests performed on the PP mesh and on the geotextile. The specimen is clamped onto a frame, which is connected to a load cell and the vertical displacements are measured using two opposite LVDTs. **b** Force–strain curve obtained for the PP mesh

A non-woven geotextile with a weight of 17 g/m^2 was installed on the side banks to retain fine materials. It was assumed that this would not affect the tensile strength of the reinforcement, both due to its low weight and the fact that it was installed in small sections of length equal to 50 cm, preventing it from contributing actively to the structural resistance.

Referring to the soil, the grain size curve, shown in Fig. 4a, was selected with limited fine content and a maximum diameter of 2 cm to represent a soil suitable for the construction of embankments. The choice of the soil, which is similar to the one adopted for the real RPEs, provides a quasi-null cohesion.

2.1.1 Construction of the RE-RPEs

Two 4-m-long embankments were constructed simultaneously at the same site, confined between two walls made of concrete blocks (Fig. 5). Wooden frames matching the cross-section of the RE-RPE were installed, and the eight layers of the embankments were assembled using formworks made from timber boards screwed to the frames as support during the construction phases. The formworks were removed at the end of the construction.

For each layer, the real width of the reinforcement panels (geogrid/DT and formworks) was accurately reproduced to account the frequency of the discontinuities. Both the real reinforcement systems have a width of $w = 3$ m; therefore, each layer consisted of six elements, each 67 cm wide (formwork and PP mesh).

The construction sequence for each layer is detailed in the following. First, the formworks (67 cm wide) were placed on the side banks by positioning them side by side, and the non-woven geotextile was attached (Fig. 6a). Next, the PP mesh panels, pre-cut to a width of approximately 70–75 cm and the appropriate length for the layer, were laid on the bottom of the layer and wrapped beyond the formworks. In the System B, clips were added with a spacing of about 4 cm according to the prescription of the product, while for the System A, the mesh panels were simply overlapped by a few centimeters. The layer was then filled with soil and compacted using a vibrating plate. The intensity and duration of the vibration were calibrated to achieve a dry soil density of at least 95% of the Proctor value, as measured by the sand cone method (ASTM D1556 2015). The mesh was wrapped to close the layer, with a flap length

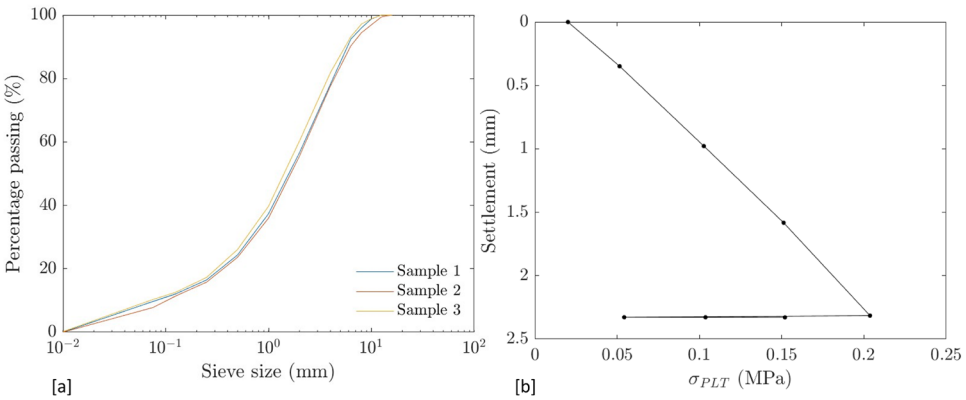


Fig. 4 **a** Granulometric curves obtained from three sample of the used soil. **b** Pressure–settlement curve obtained from a plate load test performed on a layer according to the standard (CNRBU 146/92 1992) using a plate of 30 cm



Fig. 5 Construction of the two scaled RE-RPEs: on the right is the System B, with clips and on the left is the System A, without clips



Fig. 6 **a** The positioning of the L-shaped formworks simply placed side by side. **b** The side face of the System B, from which it is possible to appreciate the rectangular formworks and the connections with clips in the four directions. **c** The hydraulic jack set-up to perform the horizontal trust

of $L_W = 25$ cm, before proceeding to the next layer. Figure 6b shows a detail of the side bank of the System B, where the clips connecting each formwork in all four directions, as well as the underlying PP mesh.

The mechanical properties of the soil were evaluated using the plate load tests (PLT) (CNRBU 146/92 1992). The load curve and corresponding settlements are shown in Fig. 4b. The compression modulus, determined between pressures of 0.15 MPa and 0.05 MPa, was 24.2 MPa.

2.1.2 Quasi-static Tests

As previously mentioned, to investigate the energy dissipating mechanism of the RE-RPEs, the effects on the displacement field caused by a block were studied under pseudo-static conditions. Specifically, a circular steel plate (30 cm in diameter) was pushed horizontally at about mid-height of the upslope side bank of the embankment through an hydraulic jack firmly constrained to a fixed support. This last had a piston stroke of 36 cm, equipped with different extensions to achieve a maximum stroke of approximately 1 m.

Specifically, the plate centre was positioned 68 cm from the base, affecting layers n°5, n°6, and the upper 2 cm of layer n°4. The layers n°7 and n°8 (top layers) were not directly influenced by the plate. A pressure transducer (sampling rate: 5 Hz) recorded the pressure in the hydraulic circuit, while the stroke advancement, therefore the upslope displacement δ_u, was manually measured with meter fixed to the jack. The advancement was documented with a camera and post-synchronized with the pressure data. In addition, the tests were continuously monitored using a photogrammetric network positioned on the downslope side to capture the embankment deformed shape over time. Further details are provided in Sect. 2.2.

As the plate load speed was very low, the inertia contribution on the energy dissipating mechanism was completely neglected. However, this test allows following step by step the displacement field created by a block during its penetration into the structure until collapse was reached. Collapse was defined by the authors as the point at which the structure exhibited a significant loss of resisting strength, which approximately coincided with the onset of soil leakage from the embankment. This point is further detailed in Sect. 3.2. This approach allowed for the observation of the energy dissipating mechanisms as a function of the reinforcement technology and provided a physical representation of the pre-collapse condition in both cases.

2.2 Photogrammetric Survey and 4D Reconstruction

Topographic measurements are frequently used in FEM back-analysis as a calibration tool for adjusting model parameters related to geometry, deformation, and initial conditions of the study system (Zhao et al. 2019; Alfio et al. 2022). These methods offer precise and reliable measurements, thanks to advanced technological equipment and robust stochastic analysis techniques (Sestras et al. 2022). Various methods, ranging from traditional surveys to active lidar acquisition and photogrammetric reconstruction, are selected based on environmental conditions, required accuracy, data density, and temporal resolution.

Scene reconstruction throughout the tests remains challenging for accurate metric measurements due to stringent data acquisition requirements and trade-offs between acquisition time and spatial resolution (Belcore et al. 2020). While lidar sensors provide high spatial resolution and dense point clouds, they are unsuitable for scenes due to their computational demands. Time-of-flight (ToF) cameras, which use active light projection, are less computationally intensive and therefore more appropriate for dynamic scenes, though they have lower depth resolution and higher noise levels at close range (Niezrecki et al. 2020).

Passive vision sensors, such as cameras, enable displacement tracking via video acquisition and can reconstruct 3D models through triangulating matching feature points across multiple cameras observing the same object. This photogrammetric reconstruction method, facilitated by modern optical sensors, ensures accurate geometric modeling along with dense point clouds and radiometric fidelity.

In this study, a 4D photogrammetric reconstruction approach combined with topographic surveying was employed. The goal was to reconstruct the RE-RPEs downslope side bank as a precise 3D model and to compare it with the FEM model for back-analysis. An optimized photogrammetric workflow was developed based on the specific requirements of this research, as outlined below. To calibrate the FEM model, an accurate reconstruction of RE-RPEs geometry and displacements during the quasi-static test was essential. An accuracy tolerance of 2 cm was set and verified with a total station survey on well-defined markers on the embankments. The target frame rate was set to 1 fps to capture dynamic scenes, balancing temporal resolution with equipment limitations. Constraints on sensor costs and the number of cameras were also considered during planning. A Sony DSX-RX0M2 compact action camera was selected considering the field condition in terms of climate and light. It features a 13.2 mm × 8.8 mm Exmor RS CMOS image sensor, and a Zeiss Tessar T* lens with a fixed focal length of 7.9 mm and an 84° field of view. The camera's small size and ability to synchronize multiple units via Wi-Fi made it ideal for this setup. Establishing a relationship between the model reference system and the measurement reference system is crucial for 3D reconstruction. This alignment was achieved using identifiable markers whose coordinates were measured in both real and reconstructed models. Sixteen checkboard markers were affixed to the downslope side bank (eight for each embarkment), measured with a total station, and used to verify the model accuracy (Fig. 7).

Three cameras were positioned 4 m from the embankment with sufficient frame overlap, achieving an average ground sample distance (GSD) of 5 mm. It is worth highlighting

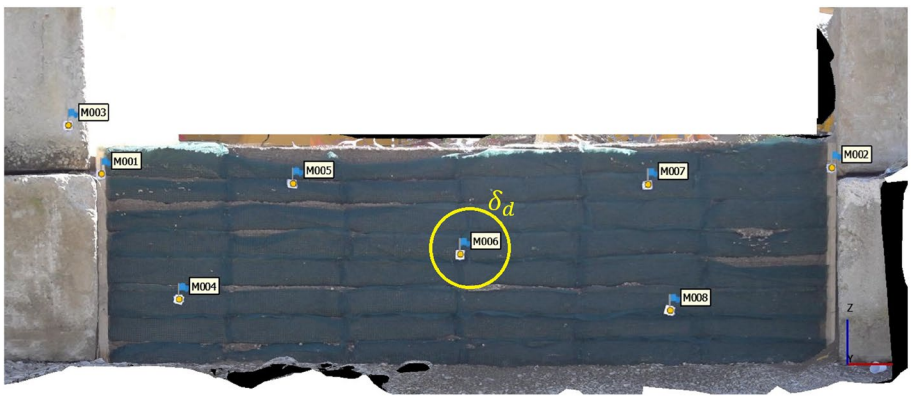


Fig. 7 Checkboard markers location on the System A downslope side bank. Marker M006 has been located opposite to the hydraulic jack position

that an accurate camera positioning is essential for reconstructing detailed 3D surfaces, enabling the production of a mesh or a digital elevation model (DEM) that could be textured for photorealistic visualization and exported for further analysis. Even in quasi-static conditions, camera synchronization is crucial to ensure consistent frame alignment over time. Using the built-in multi-camera synchronization of the camera, a smartphone app was used to trigger acquisition across all cameras simultaneously. To minimize clock drift, videos were recorded at 25 fps in a 16:9 aspect ratio and 1920x1080 resolution, saved as MP4 files with AVC encoding. For the pre-processing phase, the frames were extracted from video files using a custom MATLAB code. For this study, one frame per second was selected, balancing temporal resolution with computational efficiency. The extracted frames were processed in Agisoft Metashape ver. 1.8.4, a photogrammetric software capable of handling dynamic scenes from synchronized, statically-mounted cameras Agisoft (2024), on a system equipped with an Intel(R) Core(TM) i7–7800X CPU at 3.50 GHz, an Nvidia Quadro P1000 GPU, and 96 GB of RAM. Each camera's frames were loaded into the software, which produced a series of 3D textured models of the RE-RPE. The processing step involved aerial triangulation and bundle block adjustment to identify and match feature points across images, forming a tie point cloud that established the camera positions. The generated tie point cloud served as the basis for creating depth maps, which were subsequently used for 3D model construction. A dense point cloud through stereo matching, which could be segmented for specific analyses or used as an alternative basis for model reconstruction.

The accuracy of these models was validated by comparing the 3D RMSE on the measured markers. Six models representing six different timestamps during the quasi-static test were selected for FEM model calibration. After aligning both the photogrammetric and FEM models to the same reference system, a one-directional mesh-to-mesh distance comparison was conducted and statistically validated.

2.3 FEM Numerical Model of Reinforced Earth Embankments

The tests were numerically modeled with Abaqus/Explicit XFEM code. The model faithfully reproduced the layered structure of the embankments, the wrapped-around geometry of the reinforcement, the formwork, and, where present, the clips. The compacted soil layers and the base foundation were modeled with three-dimensional elements (C3D8R), and a linear elastic behavior associated with the Drucker–Prager yield function to model a pressure-dependent plasticity was used for the soil constitutive law (Vigna et al. 2023), as adopted in the numerical models developed by Ronco et al. (2009) to back-analyze the tests conducted by Peila et al. (2002, 2007, 2011), Ronco et al. (2009), and Ronco (2010). For the adopted constitutive model of the compacted soil, the relevant mechanical parameters are the Young's modulus E, the Poisson's ratio ν, the flow stress ratio K (i.e., the ratio of the yield stress in the triaxial tension to the yield stress in triaxial compression and, thus, controls the dependence of the yield surface on the value of the intermediate principal stress), the friction angle ϕ, the dilatancy ψ, and the cohesion c. According to what is reported in Vigna et al. (2023), the parameters were calibrated through the results of PLT test. The base foundation soil can be assumed to be significantly stiffer compared to the RPE and with the same constitutive law of the soil layers. For this reason, the Young's modulus should be set to a value an order of magnitude higher than that of the compacted soil. Although their calibration will be discussed in greater detail in Sect. 3.3, the mechanical parameters of the compacted soil and the foundation soil used in the FEM model of the reduced-scale tests are summarized in Tables 3 and 4, respectively.

Table 3 Mechanical parameters for the compacted soil constitutive law

Linear elasticity		Modified Drucker–Prager			
E [MPa]	ν [−]	K [−]	ϕ [°]	ψ [°]	c [kPa]
15	0.25	0.78	30	0	5

Table 4 Mechanical parameters for the constitutive law of the base foundation soil

Linear elasticity		Modified Drucker–Prager			
E [MPa]	ν [−]	K [−]	ϕ [°]	ψ [°]	c [kPa]
200	0.25	0.78	35	0	50

The reinforcement in PP mesh (representing both geogrid and DT mesh) was modeled as shell elements (S4RS) with elasto-plastic behavior associated with the ductile damage constitutive law. The average force–displacement curve (Fig. 3b) was implemented directly into the constitutive law, with values converted from engineering strain to true strain. Yielding was defined as the point where, after the initial phase of testing, the tangential Young's modulus becomes constant, with $E = 26.2$ MPa and Poisson's ratio set at $\nu = 0.25$. The ultimate true strain derived from the curve was $\epsilon_{max} = 0.12$. The representativeness of these values was assured by numerically modeling the laboratory tensile tests on the reinforcement. The contribution of the geotextile was neglected, being its function limited to fine-retention. This modeling approach allows managing the large deformations experienced by the shell elements: where a mesh element reaches its maximum strain, it is removed from the analysis

to simulate material local failure. The steel formworks are modeled along the shell side banks as equivalent shells with an elastic-perfectly plastic constitutive law. In the shell definition, B450C steel bars, uniformly spaced at 13 mm in both directions on the side bank, are included. Therefore, the shell mechanical properties on the side banks are derived from a homogenization process that integrates the reinforcement and steel bars into a unified model. The effectiveness of this process has been evaluated during the back-analyses of the reduced-scale tests, as reported in Sec. 3.3.

In the RE-RPEs simulating the System B, the clips were modeled as "fastener" elements within the Abaqus framework, representing local connections between elements. Specifically, they were simulated as hinge joints, with a maximum tensile strength of $F_{max} = 40$ N. When this threshold force is reached, the individual fastener element is removed from the analysis to simulate its failure. Due to the ductile damage criterion applied to the reinforcement, the model could also simulate the failure of the mesh (tearing) surrounding the clips. The occurrence of either failure mechanism depended on the relationship between F_{max}, the mechanical properties of the reinforcement, and the loading conditions. Interactions between bodies in the model were handled using the Penalty algorithm (Dassault Systèmes 2024) with a single tangential friction coefficient μ. This last has been calibrated during the back-analysis process as reported in Sec. 3.3.

The steel plate was modeled as a perfectly rigid body within the analysis. Once the gravity load was applied to the model, the plate was pushed slowly toward the upslope side bank to avoid introducing inertial effects.

3 Reduced-Scale Test

In this section, the results of the experimental campaign are detailed and presented. Special focus is given to the differences in the energy dissipating mechanisms obtained for the two technologies.

3.1 3D Digital Model from 4D Photogrammetric Processing

The methodology outlined in Sect. 2.2 enabled the precise temporal reconstruction of both embankments during the quasi-static test, yielding a valuable reference dataset for FEM back-analysis. First, a tie point cloud that established the camera positions was formed (Fig. 8a). Then the stereo matching between the cameras provided the dense point cloud (Fig. 8b) which was segmented (Fig. 8c). A series of 3D textured digital models and point clouds at each timestamp were produced. Six key timestamps, designated as T0 to T5, were selected to represent significant moments during the test and are presented as reference points (Fig. 8d). Tables 5 and 6 summarize the primary characteristics of the reconstruction for both embankments. The reconstruction accuracy was assessed by calculating the root mean squared error (RMSE) between the measured control point coordinates and those estimated during photogrammetric processing. From the 16 checkerboard markers (8 on each embankment), 6 uniformly distributed points were selected to evaluate the reliability of the multi-temporal photogrammetric reconstruction. Two of these were positioned on the lateral fixed concrete walls, which were confirmed to be free from deformation, while the remaining four were placed along the embankment edges in areas where deformation was confidently considered negligible. This selection is supported by the results: the RMSE values for these six control points remained consistently stable, i.e., below 2 cm, throughout the test, as reported in Tables 5 and 6, confirming their suitability as stable reference points. For System A, the mean error over the observed timestamps was approximately 1.23 cm, with a standard deviation of 0.059 cm. For System B, the mean error was approximately 1.01 cm, with a higher standard deviation of 0.34 cm, attributed primarily to an increase observed at T5.

The photogrammetric model exhibited stability in terms of resolution, point density, and dense cloud detail throughout the test period. Minor variations in reprojection error and RMSE indicated effective handling of deformation, although a slight decrease in control point accuracy was noted towards the final timestamp. Overall, the method demonstrated robust performance, effectively tracking deformations and maintaining model integrity. These results confirm the suitability of the proposed photogrammetric approach for monitoring subtle changes in object geometry over time.

3.2 Results of the Reduced-Scale Test

Figure 9 illustrates the displacements of the system during the tests, when the displacement imposed on the plate reached approximately 30 cm, while Fig. 10 presents the post-collapse condition.

From a macroscopic perspective, both systems with or without clips demonstrated a similar energy dissipating mechanism. From the initial stages of testing, a comparable tensile cracking pattern emerged on the crest of both embankments, defining an impact-disturbed zone (IDZ) with the shape of a truncated prism (Fig. 11). This zone was outlined upslope by the width of the plate and expanded towards the downslope bank at an angle $\psi \approx 45°$. The layers directly pushed by the plate (4, 5, and 6 starting from the base) slid downslope during the loading process. Conversely, the upper layers (7 and 8) experienced minor downslope movement. In particular, within the System B, the upper layers exhibited less movement compared to those in the System A, likely

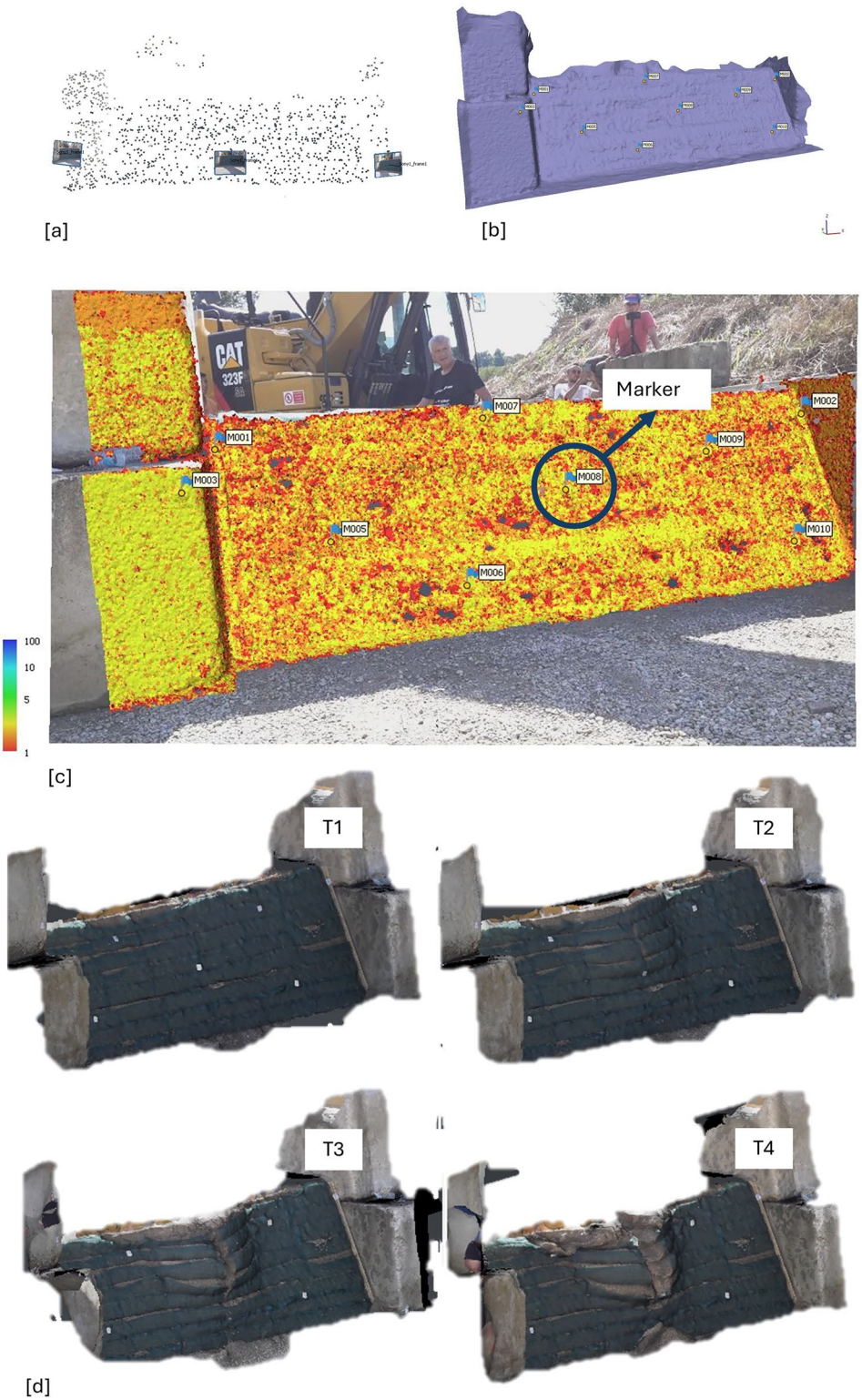


Fig. 8 **a** Camera pose estimation and reconstructed model sparse cloud. **b** Triangulated mesh. **c** Dense point cloud reconstruction with markers. The one highlighted represents that is used to evaluate the downslope displacement **d** evolution of deformation from T1 to T4

due to the influence of the clips, which contributed to a more uniform shell effect across the formworks on the downslope bank. Figure 10a illustrates how the formworks in layers 7 and 8 remained connected during the thrust, unlike the separation observed in the geogrid configuration. Nevertheless, the collapse condition and the extension of the IDZ observed after collapse were very similar in both cases (Fig. 10). These considerations are supported by the photogrammetric restitution presented in Sect. 3.4.

Table 5 Summary of photogrammetric reconstruction characteristics at different timestamps for the System A, i.e., without clips

	Time [s]	GSD [mm/pix]	Tie points [n°]	Reprojection error [pix]	Control point RMSE [cm]	Resolution [cm/pix]	Point density [pts/cm^2]	DPC [n°]	Vertices [n°]
T0	1	2.35	1155	0.602	0.86	1.14	0.766	481242	28901
T1	17	2.37	1348	0.637	0.87	1.12	0.798	493955	30208
T2	36	2.35	1163	0.675	0.88	1.12	0.795	508198	30310
T3	61	2.34	1384	0.663	0.83	1.12	0.792	515599	30224
T4	63	2.33	1233	0.632	0.83	1.11	0.817	522120	30700
T5	90	2.32	1286	0.608	1.76	1.05	0.915	509208	34810

Table 6 Summary of photogrammetric reconstruction characteristics at different timestamps for System B, i.e., with clips

	Time [s]	GSD [mm/pix]	Tie points [n°]	Reprojection error [pix]	Control point RMSE [cm]	Resolution [cm/pix]	Point density [pts/cm^2]	DPC [n°]	Vertices [n°]
T0	5	2.52	1235	0.629	1.18	1.15	0.755	366540	29860
T1	20	2.51	1244	0.675	1.14	1.13	0.779	377,626	30,421
T2	48	2.49	1187	0.596	1.23	1.14	0.771	389,111	30,539
T3	84	2.51	1274	0.672	1.24	1.12	0.793	394,618	31,835
T4	96	2.49	1156	0.602	1.25	1.32	0.572	392,294	18,397
T5	110	2.49	1058	0.657	1.33	1.13	0.785	400,492	31330

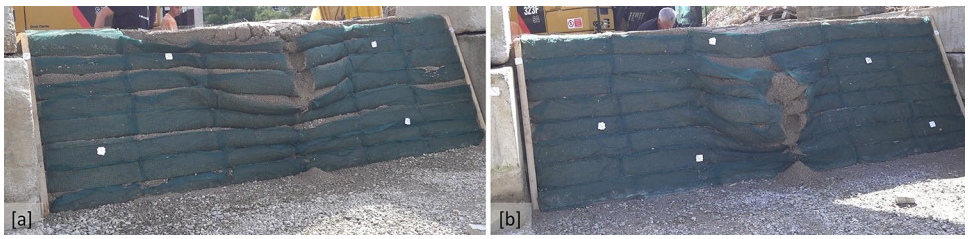


Fig. 9 Final configuration, an instant before the collapse, for System A (**a**) and System B (**b**)

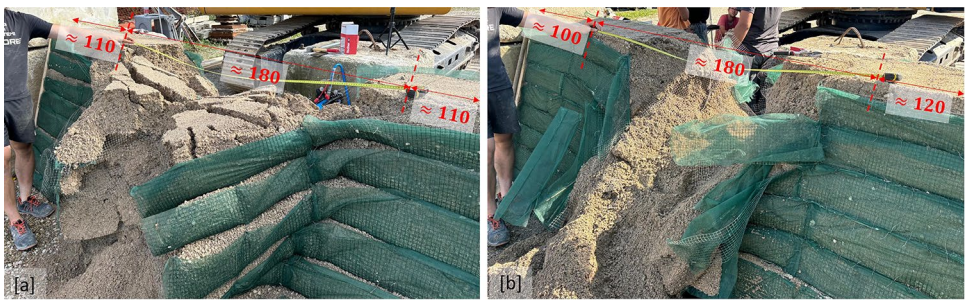


Fig. 10 Configuration after the collapse for System A (**a**) and System B (**b**)

The IDZ shapes and the energy dissipating mechanisms observed are in both cases comparable with that observed by Peila et al. (2007) during the full-scale dynamic test, i.e., downstream sliding of the involved layer. It is interesting to note that the crack patterns that originated during the test are similar to the ones observed in the full-scale tests, although in the present quasi-static tests, the inertia contribution was missing.

The force–displacement curves obtained from the post-processing of the test data are presented in Fig. 12. The δ_u values were determined in the position of the hydraulic jack with a discretization of 1 cm. Both curves exhibit a steep initial ramp spanning the first few centimeters, reaching a maximum force of approximately 12 kN. After this peak, the curves enter a plateau-like trend, indicating, in a macroscopic view, perfectly plastic behavior. This phase, in which



Fig. 11 Tension crack pattern developed on the top of both embankments. The photo refers to System B

the embankments maintain an almost-constant resistance despite increasing displacements, continues up to around $\delta_u = 18$ cm for System A. Beyond this point, the embankment shows a progressive linear decrease in the resisting force as the displacement increases. In contrast, System B maintains a constant resistance up to $\delta_u = 28$ cm. Beyond this displacement, a sharp drop in resistance was observed.

In terms of resistance, both embankments exhibit similar behavior; however, System B sustains its full resistance over a wider range of displacement. Furthermore, System B experiences an abrupt drop in resistance as δ_u increases, whereas System A shows a more gradual linear reduction. Based on the cases investigated, we observed that soil leakage and the initiation of collapse propagation typically occurred when the applied force had decreased to approximately 75% of its peak value. For this reason, we propose defining the pre-collapse condition as the displacement corresponding to 75% of the maximum force, once the peak has been surpassed. Although this threshold may serve only as an initial approximation, it is important to note that collapse does not occur precisely at the peak force, nor when the sliding displacement equals the length of the reinforcement flap. In particular, the failure displacements are determined to be $\delta_{u,f} = 36$ cm for both systems, being the flap equal to 25 cm.

3.3 Calibration of the Numerical Model

The reduced-scale tests were numerically modeled as described in Sect. 2.3. The values of the mechanical parameters of the soil, reinforcement, and clips, reported in Sect. 2.3, were determined by numerically replicating the tests used to define the key properties of each component. The properties of the elements were adjusted so that the numerical outputs closely matched the values obtained from the experimental tests. As detailed in Sect. 2.3, the reinforcement was modeled to replicate the tensile test results presented in Sect. 2.1 and Fig. 3, while the soil parameters were calibrated to match the PLT test outcomes. Given the number of parameters required by the constitutive model, the selected set (Tables 3 and 4) was chosen from combinations that aligned with the PLT data, ensuring consistency with typical values for embankment soils (Banjac et al. 2004; Chai et al. 2002; Mokhtari and Kalantari 2019; Naeini and Taherabadi 2015; Teodoru and Toma 2009; Wersäll et al. 2022; Zhou et al. 2016). As reported by Vigna et al. (2023), the Young's modulus E, the friction angle ϕ, and, to a lesser extent, the cohesion c are the parameters that most significantly influence the results and, thus, those to that more attention was paid, leaving a null dilatancy ψ and a poisson ratio $\nu = 0.25$ (Amaral et al. 2011; Patel et al. 2018). The flow stress ratio K is responsible to modify the shape of

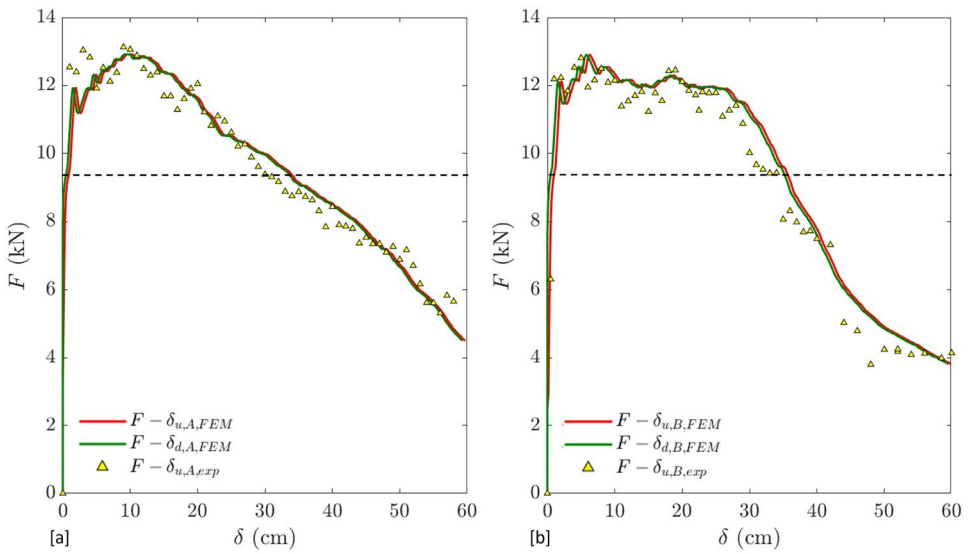


Fig. 12 Force–displacement curves obtained experimentally and with the numerical model for System A (**a**) and System B (**b**)

the yield surface, introducing rounded corners that mimic the Mohr–Coulomb criterion while preserving smoothness (Lode angle dependency) to mitigate the overestimation of strength often associated with the classical Drucker–Prager model (Mohammadi et al. 2019). As suggested also by Dassault Systèmes (2024), a value of $K = 0.78$ was selected to maintain the convexity, to maintain convexity of the yield surface, which is more suitable for modeling soil behavior (Alejano and Bobet 2014). This choice is consistent with previous studies (Peila et al. 2007; Ronco et al. 2009; Ronco 2010).

The response of the assembly to the transverse load was validated through: (i) the force–displacement curves ($F - \delta_u$) obtained from the reduced-scale tests for the upslope side, and (ii) the deformation reconstructed through photogrammetry on the downslope face. During the back-analysis process, the tangential friction coefficient value to be adopted in the Penalty algorithm for body interactions was calibrated to $\mu = 0.5$. As for the soil parameters, although the selected value represents a numerical approximation, it was chosen within the ranges typically observed for soil–geogrid interaction (Bergado et al. 1993; Zou et al. 2012; Rajesh and Viswanadham 2015). This choice was made with specific reference to the adopted materials, acknowledging that such values can vary depending on the type of both soil and reinforcement (Zou et al. 2012). It is important to note that numerical values may not perfectly replicate real-world behavior, as they are influenced by model assumptions, simplifications, and calibration procedures. Figure 12 shows the force–displacement curves obtained from the experiments and the numerical model for both tests, demonstrating good agreement in both cases. Figure 13 compares the deformed configurations between the numerical model and the photogrammetric model for System A, while Fig. 14 illustrates the same comparison for System B. In detail, both figures depict the displacement of the downstream face of the embankment along the x-axis (i.e., aligned with the direction of the applied force) across successive stages of plate advancement. The FEM model of the deformed embankment is shown in the central column, where each point is color coded according to the displacement discrepancy (i.e., error) between the photogrammetric reconstruction and the FEM simulation. The color bar on the left quantifies the pointwise error in meters. The percentages indicate the probability of observing a specific error value, while the orange line represents the distribution of the error across the entire downslope embankment surface. The right-hand column displays the corresponding Gaussian distribution of the error, with outliers appropriately removed, thereby providing a quantitative assessment of the model's predictive accuracy.

The summary statistics for these comparisons are provided in Tables 7 and 8. These values were computed based on discrepancies between the numerical and photogrammetric models over the downslope bank of the embankment.

The statistical analysis reveals a mean deviation of less than one centimeter, as evidenced by the good agreement shown in the comparison figures between the FEM and photogrammetric models. However, a difference of 20 cm is observed at the base of the structure, only, due to soil leakage from the layers, which resulted in material accumulation at the base (as shown in Fig. 9). This phenomenon cannot be captured by a FEM numerical model. Nonetheless, the numerical back-analysis demonstrated a strong correlation with the experimental results.

Table 7 Summary statistics of the difference between the displacements of the numerical model and the reconstructed photogrammetric model of the reduced-scale test on System A, for the timestamps reported in Table 5

Timestamp	Min [m]	Mean [m]	Median [m]	Standard dev. [m]	Max [m]	RMSE [m]
T0	−0.041	0.006	0.001	0.022	0.200	0.023
T1	−0.041	0.006	0.001	0.022	0.200	0.023
T2	−0.062	0.005	−0.001	0.038	0.200	0.038
T3	−0.106	−0.005	−0.004	0.037	0.197	0.037
T4	−0.115	−0.001	−0.002	0.044	0.198	0.044
T5	−0.154	0.001	−0.003	0.054	0.200	0.054

Table 8 Summary statistics of the difference between the displacements of the numerical model and the reconstructed photogrammetric model of the reduced-scale test on System B, for the timestamps reported in Table 6

Timestamp	Min [m]	Mean [m]	Median [m]	Standard dev. [m]	Max [m]	RMSE [m]
T0	−0.074	−0.008	−0.008	0.029	0.190	0.030
T1	−0.073	−0.001	−0.003	0.028	0.193	0.028
T2	−0.073	−0.005	−0.010	0.032	0.198	0.032
T3	−0.070	−0.010	−0.014	0.030	0.199	0.031
T4	−0.091	−0.010	−0.015	0.035	0.187	0.036
T5	−0.199	−0.005	−0.014	0.053	0.200	0.053

3.4 Comparison of the Energy Dissipating Mechanisms

Figure 15 shows the energy distribution from the numerical model in the RE-RPEs as a function of the δ_u imposed by the plate. It is worth highlighting that, although it is possible to extract the embankment internal energy, comprising the recoverable elastic strain energy, the energy dissipated through inelastic processes (e.g., plasticity), the energy dissipated through viscoelasticity or creep (e.g., damping mechanisms), and the artificial strain energy (e.g., due to hourglass resistances), the elastic and plastic energy components were isolated. The difference between their sum and the total internal energy was found to be less than 4%, thereby indicating that energy dissipation due to numerical modeling artefacts was limited. The energy dissipated by friction can be extracted separately; however, it encompasses all sources of friction. This includes not only the sliding between impacted layers but also the movements and oscillations occurring at the foundation level. This consideration is particularly relevant also in simulations of dynamic impacts, where friction between the block and the RPE can develop. In contrast, the contribution of frictional energy dissipation is comparatively minor in quasi-static conditions. Figure 15a illustrates, thus, the values of strain (elastic), plasticization, and frictional energies, namely E_s, E_p, and E_f, over the upslope displacements. These values are comparable between the systems, with System B dissipating a lower proportion of energy through frictional mechanisms than the System A, offsetting this difference with higher plastic energy. It is interesting to note that plasticization and frictional energies are monotonically increasing, while strain energy, which is recoverable, can reduce. Figure 15b reports the partitioning of the three different energies. At each displacement, the summation of the three energies is always equal to 1.

As highlighted in Fig. 15b, after the initial displacement, E_f and E_p of System A stabilize at approximately 80% and 15%, respectively. System B exhibits an E_f range of 65–75%, with E_p progressively increasing until stabilizing at 25% for $\delta_u > 38$ cm. These results are not in contradiction with the findings of Peila et al. (2007) and Ronco et al. (2009), who reported that approximately 80–85% of the energy is dissipated through plastic deformation and 15–20% through friction, as the cases presented in those studies pertain exclusively to dynamic impact conditions. Under dynamic test conditions, similar values have also been reported from small-scale experiments by Hofmann and Mölk (2012) and Kister et al. (2017). As noted by Marchelli et al. (2022b), these values were derived from specific experimental set-ups and commonly adopted embankment geometries, and are, therefore, applicable to a specific range of reinforced protective embankments, pertaining to impact conditions only. In both System A and B, E_s remains negligible. These differences in energy distribution stem from the behavior of the clips. The higher energy dissipation by plasticization observed in System B, beginning at relatively low displacements (typically around 10 cm), can be attributed to the increased confinement provided by the presence of clips. This confinement likely results in elevated stress levels within the soil and/or an increased volume of soil subjected to high stress, thereby promoting plastic deformation from the early stages of loading. In addition, the progressive break of the clips during testing, with each break corresponding to a failure force, contributes in increasing the dissipation of energy though plasticization.

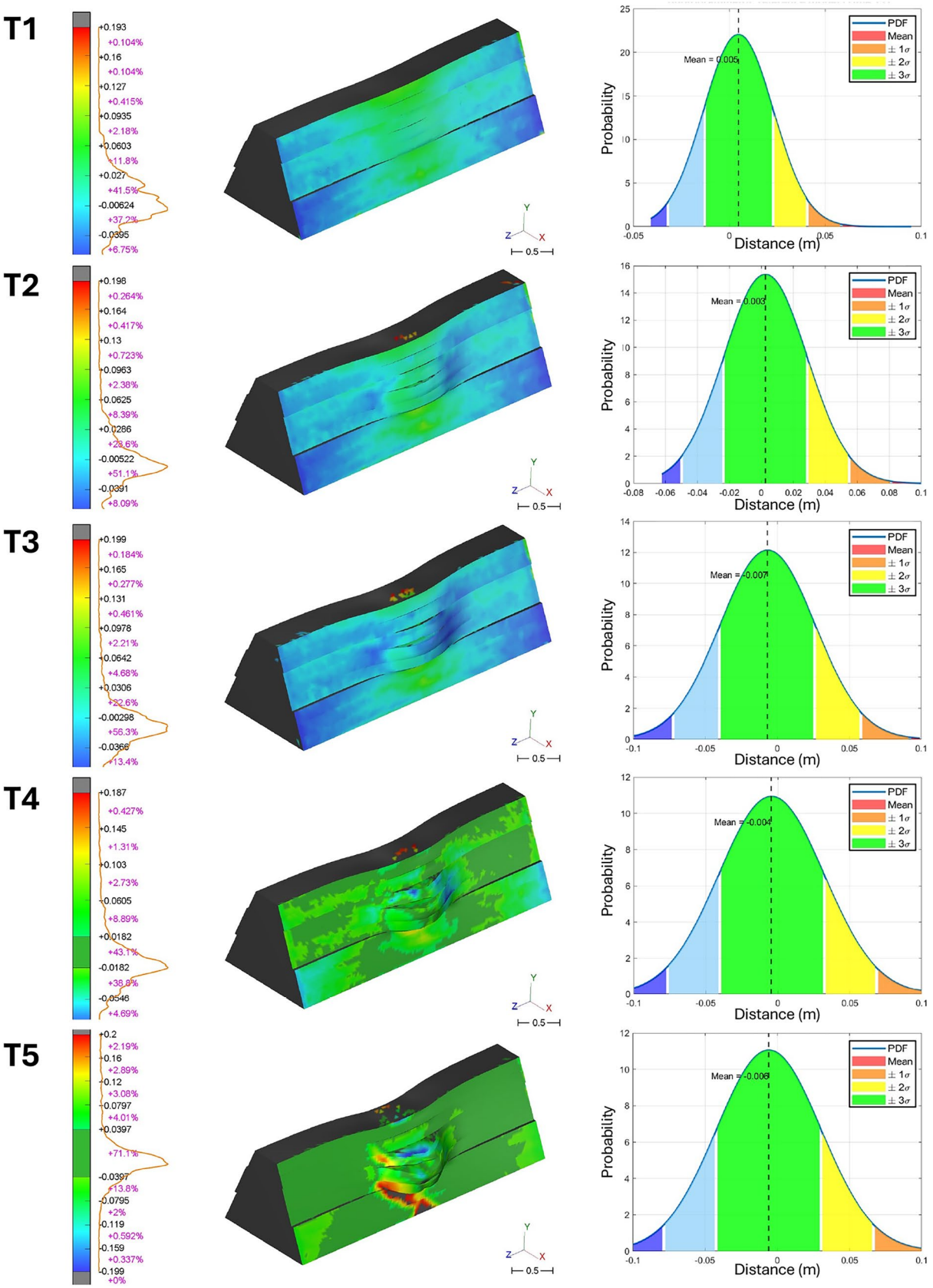
In this quasi-static case, the plastic energy constitutes a minor component of the energy dissipating mechanism, and the plastic zones are confined to the initial centimeters of the upslope face, near the plate, while large portion of the energy dissipates through friction. As mentioned in the methodology, this is a drawback of adopting a quasi-static experimental approach, rather than a dynamical modeling. This confirms the assumption in Lambert and Bourrier (2013), Lambert et al. (2014), and Marchelli et al. (2022b), i.e., that the downslope section of the IDZ functions as a buttress.

Table 9 shows the maximum tangential force, F_t, on foundation slices, calculated for a half-model with a symmetry plane passing through the plate center. These values are referenced to rectangular slices, with, for example, the case 0.25–0.5 indicating the rectangular width from 0.25 m to 0.5 m from the symmetry plane. The F_t values across the entire foundation are 10.15 kN and 11.50 kN for System A and System B, respectively.

Regarding individual slices, System B shows slightly higher F_t values, likely due to the stiffening effect provided by the additional clips. The slice at 1.5–1.75 registers an F_t value around 15% of the maximum, which can be considered negligible. This indicates an affected foundation zone approximately 10 times the plate diameter, which aligns well with the ONR 24810 guidelines suggesting an impact zone of 8–9 times the block diameter for reinforced embankments (ONR 24810 2021).

4 Suitability of the Method to Define Pre-collapse Conditions

To verify whether the force–displacement curve obtained in a quasi-static test can be used to define the downslope allowable displacements also in dynamic conditions, i.e., when an impact occurs, the real-scale test (Test $n°$ 2) presented in Peila et al. (2007) was analyzed. This test involved an RE-RPE reinforced with unidirectional geogrid (TT045 by Tenax producer) with seven layers, $b = 0.9$ m, $\alpha = 64°$ and


T1
+0.193
+0.104%
+0.16
+0.104%
+0.127
+0.415%
+0.0935
+2.18%
+0.0603
+11.8%
+0.027
+41.5%
-0.00624
+37.2%
-0.0395
+6.75%
T2
+0.198
+0.264%
+0.164
+0.417%
+0.13
+0.723%
+0.0963
+2.38%
+0.0625
+8.39%
+0.0286
+28.6%
-0.00522
+51.1%
-0.0391
+8.09%
T3
+0.199
+0.184%
+0.165
+0.277%
+0.131
+0.461%
+0.0978
+2.21%
+0.0642
+4.68%
+0.0306
+22.6%
-0.00298
+56.3%
-0.0366
+13.4%
T4
+0.187
+0.427%
+0.145
+1.31%
+0.103
+2.73%
+0.0605
+8.89%
+0.0182
+43.1%
-0.0182
+38.9%
-0.0546
+4.69%
T5
+0.2
+2.19%
+0.16
+2.89%
+0.12
+3.08%
+0.0797
+4.01%
+0.0397
+71.1%
-0.0397
+13.8%
-0.0795
+2%
-0.119
+0.592%
-0.159
+0.337%
-0.199
+0%
Y
Z
X
0.5
PDF
Mean
± 1σ
± 2σ
± 3σ
Mean = 0.005
Mean = 0.003
Mean = -0.007
Mean = -0.004
Mean = -0.008
Probability
Distance (m)

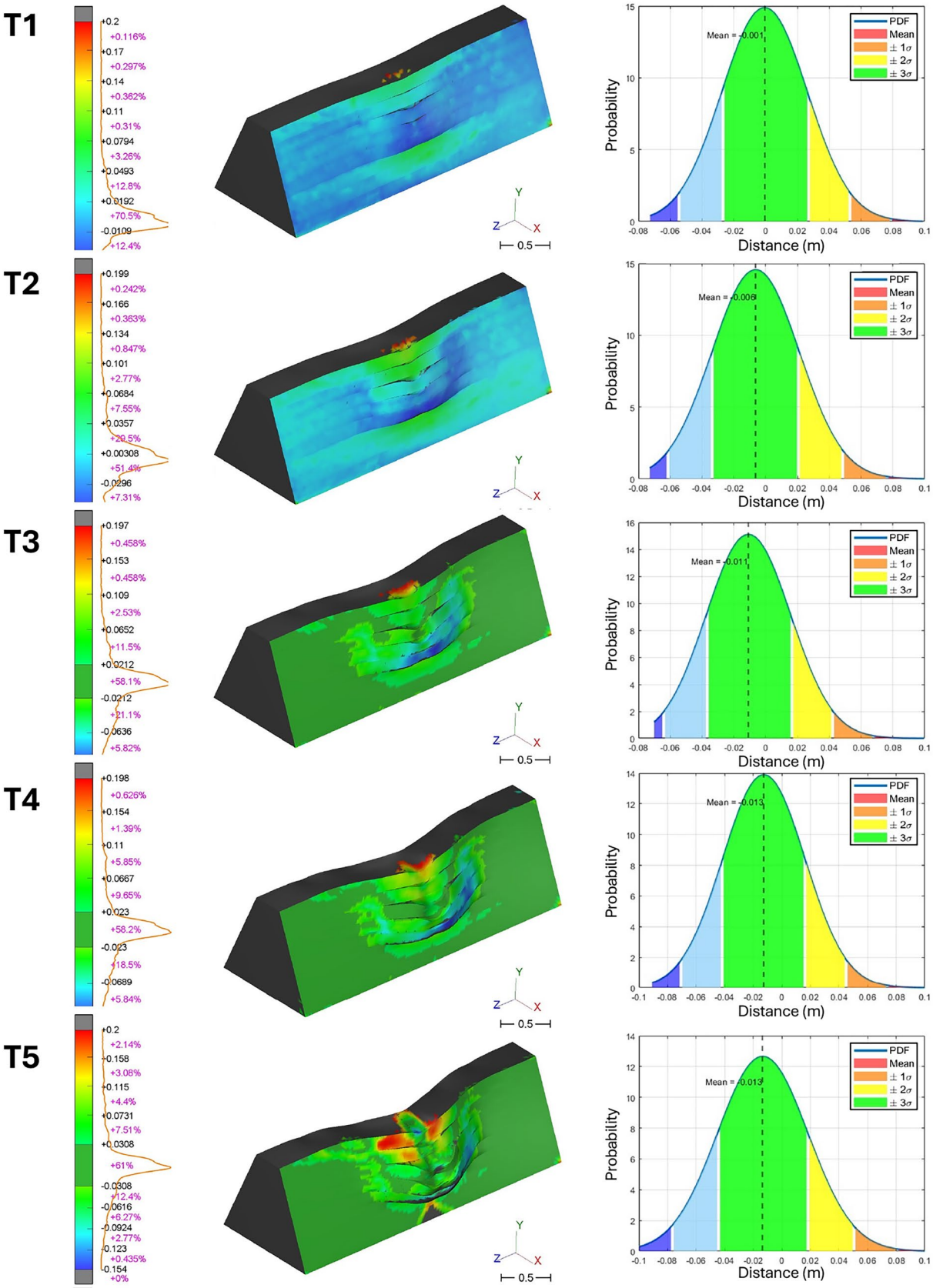
◂**Fig. 13** Comparison on the downslope side bank deformation between the numerical model results and the photogrammetric restitution for System A. The figures report the differences in horizontal displacement at various stages of plate advancement: T1 $\delta_u = 15$ cm; T2 $\delta_u = 25$ cm; T3 $\delta_u = 35$ cm; T4 $\delta_u = 45$ cm; T5 $\delta_u = 58$ cm

$H = 4.20$ m. Three consecutive impacts at $H_{imp} \approx 2.7$ m with an 8700 kg impactor at a speed of 32 m/s, nearly normal to the face, were necessary to cause the collapse of the structure. Only the upslope and downslopw maximum displacement values at the end of the test were available: the first impact caused $\delta_u \approx 0.95$ m and $\delta_d \approx 0.80$ m, while the second $\delta_u \approx 1.30$ m and $\delta_d \approx 1.20$ m. Finally, the third impact led to excessive downslope deformation, resulting in soil leakage and the collapse of the structure (Peila et al. 2002, 2007, 2011; Ronco et al. 2009; Ronco 2010).

The test was numerically modeled in Abaqus/Explicit with the same approach previously described in Sect. 2.3. In this case, the formworks, made of electro-welded metal mesh, were modeled as beam elements embedded in the soil. The impactor was simulated as a rigid sphere with $R = 0.90$ m. More details about the modeling approach under dynamic conditions can be found in Vigna et al. (2024). In this case, unlike the numerical model developed for the reduced-scale embankments, neither tensile tests on the adopted reinforcement nor PLT tests on the soil were available. For the reinforcement, only the maximum tensile strength was provided. Consequently, the geogrid properties in the numerical model were calibrated to match this single experimental value. Regarding the soil, composed of sand and gravel, only cohesion, friction angle, and density were reported from field observations. Due to these limitations, the mechanical parameters of both the individual components and the overall system were calibrated through a back-analysis of first and second impacts. This was performed by comparing the maximum absolute displacements measured at a height approximately corresponding to the centre of the block, recorded at the end of each impact in the real-scale tests. In addition, the observed sliding kinematics and the extent of the impact deformation zone (IDZ) were qualitatively matched. Accordingly, the numerical values of the soil parameters were selected to reproduce the observed displacements, with particular attention given to fixing the soil friction angle, an essential aspect of the analysis, as close as possible to the estimated in situ value. This approach is consistent with the values adopted in the only numerical model available for these tests (Ronco et al. 2009). Despite a numerical value, the Young's modulus is reasonably higher for the model representing the real-scale tests compared to the reduced-scale ones, likely due to more effective compaction achieved during full-scale construction. It is important to emphasize that the values used in the numerical model are approximations and may differ from actual physical properties due to model simplifications, calibration constraints, and the need to ensure numerical stability. For instance, a relatively high cohesion value and a non-negligible dilatancy angle were introduced in the model. While these may not fully reflect the real material behavior, they were necessary to replicate the experimental response. Finally, the soil–reinforcement interface friction angle μ was selected from typical ranges for this material combination (Zou et al. 2012), but was also adjusted numerically to ensure consistency with the observed performance, resulting in $\mu = 0.7$. Although a specific numerical value is not provided, the parameter, similarly to the Young's modulus, is reasonably higher in the model representing the real-scale tests compared to the reduced-scale ones. This difference is likely attributable to variations in grain-size distribution and the type of reinforcement used. Nevertheless, (Rajesh and Viswanadham 2015), through numerical modeling and sensitivity analyses, have found that no significant variation in the horizontal stress and strain distribution has been observed with an increase in the soil–geogrid interface friction. Table 10 reports the calibrated soil parameters. It is worth mentioning that these values differ from those reported in the numerical model by Ronco et al. (2009), particularly with reference to E. In has to be noted that Ronco et al. did not specifically modeled the reinforcement; hence, their material should account for its contribution. It should also be noted that experimental data from other impact tests on the same reinforcement technology are currently not available in the literature. Studies such as those by Mongiovi et al. (2014) or tests conducted by manufacturers have not been published or made accessible in sufficient detail. As a result, further refinement of the numerical model would benefit from additional experimental data to improve the reliability and generalizability of the adopted parameters. Figure 16a shows the final configuration in the numerical model.

A quasi-static test on the same RE-RPE geometry was numerically performed, considering a circular rigid plate with the same dimensions as the impactor ($R = 0.90$ m), pushing along the horizontal direction at the same height observed during the real-scale test. The resulting force–downslope displacement curve is reported in Fig. 16b. The force–upslope displacements curve was not reported as, pertaining to a quasi-static loading condition, it neglects the additional plasticization contribution that occurs when a dynamic collision happens. In this latter case, the evolution of the impact force would expect a well-marked peak (Labiouse et al. 1996; Pichler et al. 2005; Calvetti et al. 2005; Yong et al. 2022).

Referring to Fig. 16b, the two blue lines indicate δ_d values obtained in the real-scale test at the end of the first and second impacts, i.e., 0.80 m and 1.20 m, respectively. The black dashed line, corresponding to the 75% of the maximum


T1
+0.2
+0.116%
+0.17
+0.297%
+0.14
+0.362%
+0.11
+0.31%
+0.0794
+3.26%
+0.0493
+12.8%
+0.0192
+70.5%
-0.0109
+12.4%
T2
+0.199
+0.242%
+0.166
+0.363%
+0.134
+0.847%
+0.101
+2.77%
+0.0684
+7.55%
+0.0357
+29.5%
+0.00308
+51.4%
-0.0296
+7.31%
T3
+0.197
+0.458%
+0.153
+0.458%
+0.109
+2.53%
+0.0652
+11.5%
+0.0212
+58.1%
-0.0212
+21.1%
-0.0636
+5.82%
T4
+0.198
+0.626%
+0.154
+1.39%
+0.11
+5.85%
+0.0667
+9.65%
+0.023
+58.2%
-0.023
+18.5%
-0.0689
+5.84%
T5
+0.2
+2.14%
+0.158
+3.08%
+0.115
+4.4%
+0.0731
+7.51%
+0.0308
+61%
-0.0308
+12.4%
-0.0616
+8.27%
-0.0924
+2.77%
-0.123
+0.435%
-0.154
+0%
Y
Z
X
0.5
Mean = -0.001
Mean = -0.006
Mean = -0.011
Mean = -0.013
Mean = -0.013
PDF
Mean
± 1σ
± 2σ
± 3σ
Probability
Distance (m)

◂**Fig. 14** Comparison on the downslope side bank deformation between the numerical model results and the photogrammetric restitution for System B. The figures report the differences in horizontal displacement at various stages of plate advancement: T1 δ_u = 12; T2 δ_u = 32 cm; T3 δ_u = 45 cm; T4 δ_u = 61 cm; T5 δ_u = 68 cm

observed force (1107 kN) in the quasi-static numerical simulation, permits to evaluate the proposed value for the allowable downslope displacement $\delta_{d,all}$, resulting in $\delta_{d,all} \approx 1.8$. Despite representing a unique study case, it could be noted that this value is larger than the displacements measured during the first and second impacts, which did not result in the RPE collapse. Although this example does not validate the specific choice of the 75% peak force threshold, it clearly demonstrates that collapse occurs after the maximum force has been exceeded.

Figure 17 reports the various energy contributions in the numerical models of the quasi-static test (a) and the model that simulates the first impact of the real-case test (b). The continuous lines refer to the irreversible mechanisms (plasticization of the materials and friction), while the dashed lines are associated to the reversible mechanisms (elasticity). Figure 17a plots the energy contributions with respect to the downslope displacement in both the quasi-static and the dynamic loading conditions. As already pointed out, the dissipation of energy in the soil through plasticization is completely different from a quasi-static to a dynamic test, hence the two quantities cannot be compared. Conversely, the comparison can be done with the frictional energy of the two studied configurations. At a downslope displacement of 0.8 m, resulting from the real-scale tests and from their simulations, the energy $E_{f,QS}$ of Fig. 17a is equal to 235 kJ (bullet point).

Independently from the type of simulation, it is important to state that in the total energy decreases over time. This is due to the implementation of specific boundary conditions that simulate an infinite half-space beneath the foundation. These boundaries allow the energy to exit the numerical domain, thereby mimicking the behavior of a real geotechnical system. In the dynamic case, that is the one in which the reduction of total energy is more evident, the impacting block has initial velocity with horizontal and vertical components of 28.54 m/s and 12.09 m/s, respectively, resulting in a total velocity magnitude of 31 m/s. The corresponding total kinetic energy is 4179 kJ, which can be decomposed into two components: the horizontal component, 3543 kJ, and the vertical component, equal to 636 kJ. The analysis of the time histories of model outputs indicates that a portion of the energy exits the numerical domain and is transferred to the simulated half-space: the total energiy within the model reduces with time and is lower than the initial kinetic energy. In general, the horizontal kinetic energy is dissipated within the embankment through permanent deformations, while the vertical kinetic energy is primarily transmitted to the foundation. It is also noteworthy that the block retains small residual translational and rotational velocities, resulting in a minor amount of residual kinetic energy at the end of the simulation.

A deep analysis of the dynamic case reveals interesting insights into the energy transfer mechanisms during the collision of the block on the embankment and the subsequent sliding. To illustrate the comprehension of the phenonena, Fig. 18 is reported. The interaction between the block and the embankment can be divided into three distinct phases. The first phase (Phase 1) lasts for a few tenths of a millisecond, beginning at 248 ms and ending at 264 ms, when the elastic strain energy (recoverable energy) reaches its peak value of 328.9 kJ (Fig. 18a). During this phase, a shock wave develops within the system due to block contact. Despite the high accelerations experienced by the block, only a slight reduction in its velocity is observed (Fig. 18b). The downward displacement of the RE-RPE is limited to a few millimetres (6 mm). The second phase (Phase 2) commences at 264 ms and continues for approximately 50 ms after the initial contact, concluding at around 300 ms. During this interval, the strain energy begins to decrease, and the block undergoes further deceleration. By the end of this phase, the horizontal velocity of the block decreases from 28.54 m/s to 3.89 m/s, while the vertical velocity magnitude reduces to zero, indicating that the block is moving purely in the horizontal direction. The downslope displacement increases, and at 300 ms, the velocity of the downslope control point becomes comparable to that of the block. This synchronization of motion marks the end of Phase 2, signifying that the momentum of the impacting mass has been transferred to the embankment. The third phase (Phase 3) involves the deceleration of both the block and the embankment. During this phase, friction between the layers dissipates the kinetic energy of the moving masses (IDZ and block). Referring specifically to the energy dissipated by friction, a sudden increase in the blue curve of Fig. 17b is observed despite a nearly zero displacement. This rise occurs within the first tenths of a millisecond of interaction, corresponding to Phase 1. This initial energy rise is attributed to the friction generated between the block and the RE-RPE and not to the sliding between the layers, as observed in the quasi-static tests. To isolate the contribution of the IDZ sliding, this portion of the energy is subtracted from the total friction energy. The subplot in Fig. 17b1 reports, in red, the new energy axes, which have been translated upwards of about 94.2 kJ. Removing the energy value corresponding to the instant at 264 ms it could be observed that the maximum friction energy (341.1 kJ - 94.2 kJ = 246.9 kJ) matches the value observed in the quasi-static test at the same displacement (235.6 kJ), with an error of 5%, roughtly.

As a result of this analysis, the similarity between quasi-static and dynamic that is observed in the displacement field also emerges from an energetic point of view.

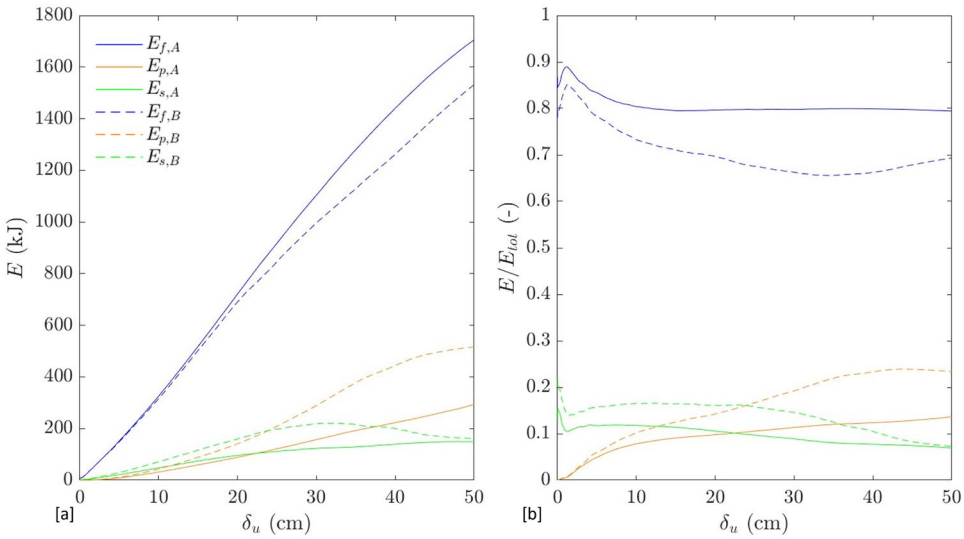


Fig. 15 Energy contributions of the RE-RPEs obtained with the numerical back-analysis. "**a**" and "**b**" indicate, respectively, System A and System B

Table 9 Maximum tangential force F_t obtained on slices of the foundation, computed in symmetric condition respect the center of the plate: e.g., 0–0.25 means the slice from 0 m (center of the plate) to 0.25 m wide

Slice [m]	System A [kN]	System B [kN]
0–0.25	1.90	1.99
0.25–0.50	1.58	1.70
0.50–0.75	1.42	1.53
0.75–1.00	1.16	1.34
1.00–1.25	0.98	1.08
1.25–1.50	0.57	0.78
1.50–1.75	0.22	0.30
1.75–2.00	0.07	0.06

Table 10 Mechanical parameters for the compacted soil constitutive law

Linear elasticity		Modified Drucker–Prager			
E [MPa]	ν [−]	K [−]	ϕ [°]	ψ [°]	c [kPa]
60	0.25	0.78	35	10	40

5 Conclusion

In this work, a method for identifying the pre-collapse condition of reinforced rockfall protection embankments subjected to a lateral pushover force has been proposed. Briefly, it consists of plotting the force–downslope displacement response curve of the layered system obtained from numerical modeling, evaluating the maximum allowable displacement, and adopting this value for dynamic impact stability analyses. This assumption is based on previous findings from past field tests and numerical analyses, that have highlighted how downslope displacements are primarily due to the sliding of the volume of the embankment disturbed by the impact, with the energy dissipation mechanism relying mainly on friction.

Pushover tests were performed on reduced-scale RE-RPE conceived in such a way to guarantee a geometrical scaling of approximately 1/5. The scaling of all the other variables involved has been performed, thanks to the classical Buckingham's Π-theorem. A steel circular plate was pushed at mid-height against the upslope side of the structure with an instrumented hydraulic jack (force and displacement) until collapse occurred. A continuous photogrammetric network monitored the downslope side, enabling continuous restitution of the deformed geometry during testing. Two types of reinforcement were studied: the geogrid and the Terramesh systems. The latter includes the clips that connect reinforcement layers.

In these tests, the RE-RPE allow displacement results as the downslope displacement in the post-peak phase corresponding to force equal to 3/4 (75%) of the peak recorded force. To extend the validity of these observations also to dynamic impact cases, the reduced-tests have been modeled in Abaqus/Explicit, and the obtained force and displacement fields have been compared with the force–displacement curves recorded from the hydraulic jack. The model has been further calibrated using a photogrammetric reconstruction of the entire downslope face of the embankment, based on point cloud data acquired throughout the duration of the tests. This continuous monitoring enabled a detailed comparison between observed deformations and model predictions, enhancing the reliability of the simulation. It is important to note that the photogrammetric reconstruction yields an RMSE in the range of 1–2 cm for the control points, which is comparable to the smallest observed displacements. Consequently, this limits the reliability of quantitative assessments during the initial phases

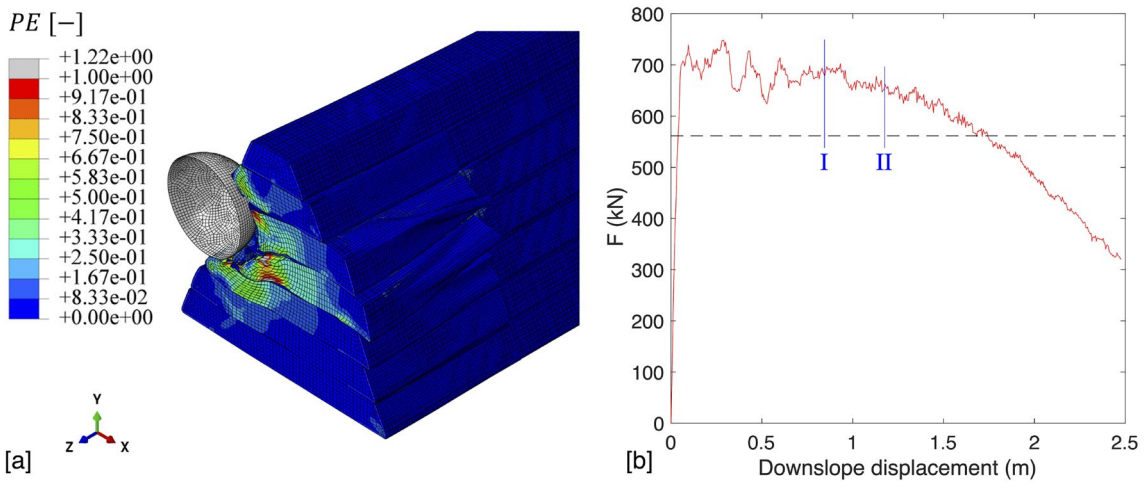


Fig. 16 **a** Back-analysis of test $n°$ 2 from Peila et al. (2007), highlighting the plastic strain (*PE*). **b** Force–displacement curve obtained for the tested RE-RPE in quasi-static conditions. The two blue vertical lines indicate the downslope displacement δ_d values obtained in the real-scale test after the first and second impacts, while a dashed horizontal line represents the 75% of the maximum force in the quasi-static test

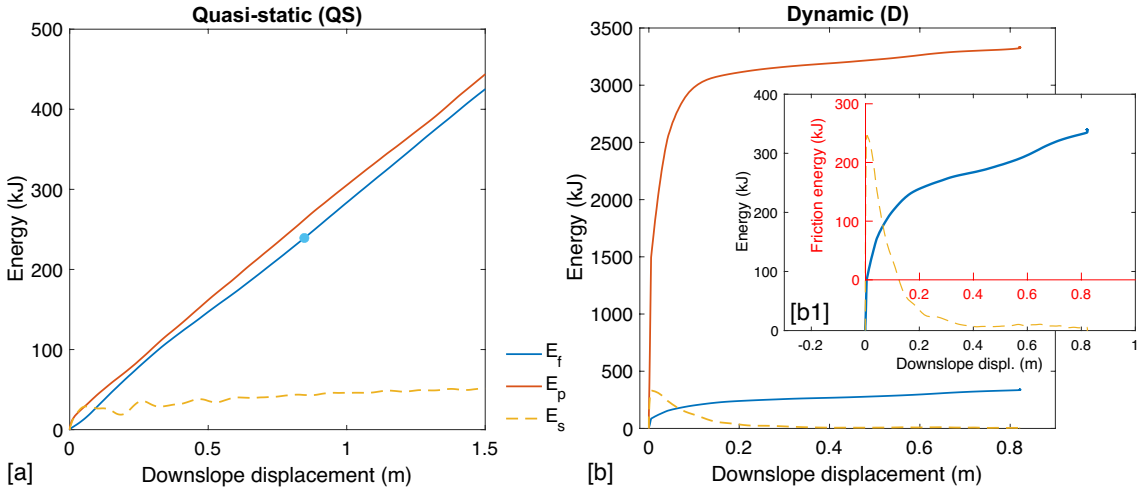


Fig. 17 The energy partitioning obtained with the numerical model of (**a**) the quasi-static (QS), and (**b**) the dynamic impact (D) tests with respect to the downslope displacement. The light-blue bullet point on the $E_{f,QS} - \delta_d$ curve marks the downslope displacement δ_d observed at the end of the first impact in the real-scale test. The subplot [b1] zooms the results of the dynamic impact tests for strain and friction energy: the translated axes refer to the reduced E_f and are reported in red. Refer to the text for the explanation

of deformation. However, as displacements exceed the measurement uncertainty, the results become increasingly robust. Despite this limitation, the control points remain the most reliable indicators of absolute model accuracy and define the domain within which the reconstruction can be considered valid ground truth for the FME modeling. The numerical model well caught the behaviors observed in the experiments: they revealed comparable energy dissipating mechanisms, with downslope sliding of the engaged layer and minor movements in the upper layers.

To investigate the compatibility of the proposed stability conditions to the dynamic impact case, a full-scale impact test has been numerically simulated by back-analyzing the test performed by Peila et al. (2007). Considering the same embankment geometry, a quasi-static test was numerically simulated and results between quasi-static and dynamic numerical tests were compared to highlight the suitability

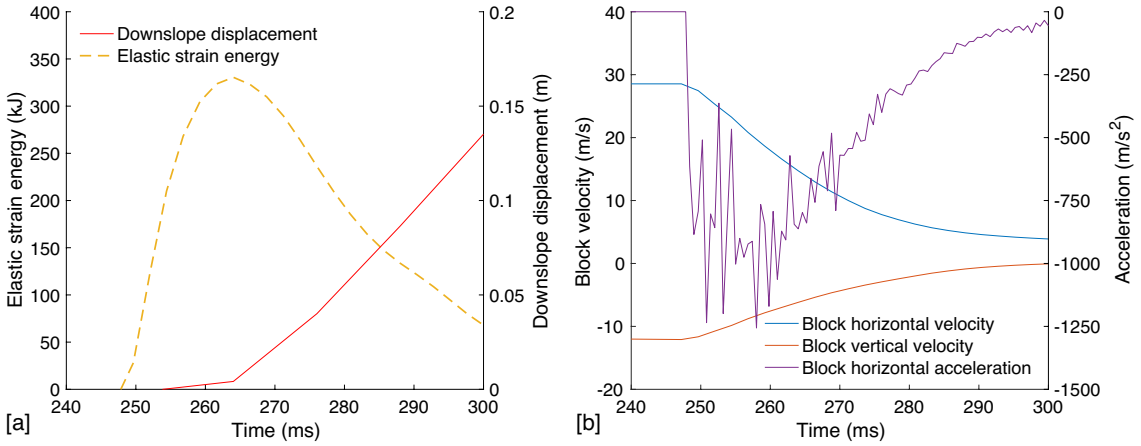


Fig. 18 Block horizontal and vertical velocities and block horizontal acceleration in Phases 1 and 2 (**a**); strain energy and downslope displacement in Phases 1 and 2 (**b**). Both figures refer to the dynamic impact case

of the approach, showing a positive agreement between downslope displacements and absorbed frictional energies. While this example does not confirm the precise validity of the 75% peak force threshold, it clearly indicates that collapse occurs after the maximum force has been surpassed.

It is necessary to mention the limitations of the work. In our study, we employ quasi-static tests to evaluate the performance of the rockfall embankment. This approach assumes a slow loading rate, thereby neglecting dynamic effects such as inertia. In addition, as the focus is on capturing the embankment's response under simplified, controlled conditions, the adopted quasi-static loading application neglects the influence of a dynamic load on the behavior of the soil in the surroundings of the impacted part. Anyway the adoption of a quasi-static testing approach allows us to isolate and analyze the energy dissipation due to friction and the resulting downslope displacements, only. Second, the valitation of the methodology lies on a limited number of tests. Further studies will address all these aspects. Nevertheless, the proposed approach simplifies the analysis by eliminating the need for dynamic modeling, making it a practical design tool.

Acknowledgements The authors thanks Andrea Carigi, Alfio Di Giovanni, Nives Grasso, Carmine Todaro, Nima Bahrami, and Davide Zanti for the help provided during the field tests. The authors also thank the reviewers, who provided interesting comments and insights, increasing the quality of the work.

Author contribution Conceptualization (S.V., M.M., V.D.B., D.P.), Methodology (all the authors), Software (S.V., V.D.P.), Validation (M.M., V.D.B.), Formal analysis (S.V., M.M., V.D.B., V.D.P.), Writing - Original Draft (S.V., M.M., V.D.B.), Writing - Review & Editing (M.M., V.D.B, V.D.P.), Funding acquisition (D.P., M.M.)

Funding Open access funding provided by Politecnico di Torino within the CRUI-CARE Agreement. This study was carried out within the project NODES which has received funding from the MUR –M4C2 1.5 of PNRR with grant agreement$$n^\circ$$ECS00000036 and within (M.M.) the Marie Curie Postdoctoral Fellowship 2022 (Call Horizon-MSCA-2022-PF-01, grant GA101103401 - RIDETHERISK project).

Data availability Data are available upon reasonable request to the corresponding author.

Declarations

Conflict of Interest The authors declare that there is no conflict of interest.

Open Access This article is licensed under a Creative Commons Attribution 4.0 International License, which permits use, sharing, adaptation, distribution and reproduction in any medium or format, as long as you give appropriate credit to the original author(s) and the source, provide a link to the Creative Commons licence, and indicate if changes were made. The images or other third party material in this article are included in the article's Creative Commons licence, unless indicated otherwise in a credit line to the material. If material is not included in the article's Creative Commons licence and your intended use is not permitted by statutory regulation or exceeds the permitted use, you will need to obtain permission directly from the copyright holder. To view a copy of this licence, visit http://creativecommons.org/licenses/by/4.0/.

References

Abu El-Soud S, Belal AM (2018) Bearing capacity of rigid shallow footing on geogrid-reinforced fine sand-experimental modeling. Arab J Geosci 11:247

Agisoft (2024) Agisoft Metashape. https://www.agisoft.com (accessed on 14 Nov 2024)

Alejano LR, Bobet A (2014) Drucker-prager criterion. The ISRM suggested methods for rock characterization, testing and monitoring: 2007–2014. Springer, pp 247–252

Alfio VS, Costantino D, Pepe M et al (2022) A geomatics approach in scan to fem process applied to cultural heritage structure: the case study of the "colossus of barletta''. Remote Sens 14(3):664

Alves M, Oshiro RE (2006) Scaling impacted structures when the prototype and the model are made of different materials. Int J Solids Struct 43(9):2744–2760

Amaral M, Viana da Fonseca A, Carvalho J, et al (2011) Dynamic poisson ratio analysis. In: Proceedings of the 15th European Conference on Soil Mechanics and Geotechnical Engineering, IOS Press, pp 115–120

Ambur D, Chunchu P, Rose C, et al (2005) Scaling the non-linear impact response of flat and curved composite panels. In: 46th AIAA/ASME/ASCE/AHS/ASC Structures, Structural Dynamics and Materials Conference, p 2224

ASTM D1556 (2015) Standard test method for density and unit weight of soil in place by the sand-cone method

ASTM D6637 (2015) Standard test method for determining tensile properties of geogrids by the single or multi-rib tensile method

Banjac R, Mayor P, Hufenus R (2004) Plate loading test on a geosynthetic renforced shallow embankment:field measurements and numerical modelling. In: Proc. EuroGeo 3, Munich, Germany, March 1-3, 2004

Belcore E, Piras M, Wozniak E (2020) Specific alpine environment land cover classification methodology: Google earth engine processing for sentinel-2 data. Int Arch Photogramm Remote Sens Spat Inf Sci 43:663–670

Bergado D, Chai J, Abiera H et al (1993) Interaction between cohesive-frictional soil and various grid reinforcements. Geotext Geomembr 12(4):327–349

Bertrand D, Nicot F, Lambert S, et al (2007) Dem modeling of a cellular structure for rockfall protection based on a multiscale approach. In: 10 th International Symposium on Numerical Models in Geomechanics NUMOG, pp 707–713

Blovsky S (2002a) Bewehrungsmöglichkeiten mit geokunststoffen. PhD thesis, Technische Universität Wien

Blovsky S (2002b) Model tests on protective barriers against rockfall. In: 15th EYGEC–European Young Geotechnical Engineers Conference

Bragonzi G, Cancelli P, Tedeschi L, et al (2016) Boulder impacts on reinforced embankments: modeling and design considerations. In: Eurogeo 6, 25/28 September 2016, Ljubljana,, pp 1–11

Breugnot A, Lambert S, Villard P et al (2016) A discrete/continuous coupled approach for modeling impacts on cellular geostructures. Rock Mech Rock Eng 49(5):1831–1848

Brunet G, Giacchetti G, Bertolo P, et al (2009) Protection from high energy rockfall impacts using terramesh embankments: design and experiences. In: 60th Highway Geology SymposiumNew York State Thruway AuthorityNew York State Department of TransportationNew York State Museum

Buckingham E (1914) On physically similar systems; illustrations of the use of dimensional equations. Phys Rev 4(4):345

Calvetti F, Di Prisco CG (2007) Linee guida per la progettazione di gallerie paramassi. Tech. rep, Starrylink Editrice Brescia

Calvetti F, Prisco C, Vecchiotti M (2005) Experimental and numerical study of rock-fall impacts on granular soils. Rivista Italiana di Geotecnica 4(4):95–109

Carotti A, Peila D, Castiglia C, et al (2000) Mathematical modelling of geogrid reinforced embankments subject to high energy rock impact. In: Proceedings of Eurogeo, II European Geosynthetics Conference and Exhibition, Bologna, Italy, pp 15–18

Carotti A, Di Prisco C, Vecchiotti M et al (2004) Modeling of geogrid reinforced embankments for rockfall protection. 3rd European Geosynthetics Conference. Munich, Germany, pp 1–3

Chai JC, Miura N, Shen SL (2002) Performance of embankments with and without reinforcement on soft subsoil. Can Geotech J 39(4):838–848

Cimellaro GP, Marasco S (2018) Introduction to dynamics of structures and earthquake engineering, vol 45. Springer

Clerici A, Giuriani E, Cambiaghi D, et al (2013) Rockfall full scale field tests. Landslide Science and Practice: Volume 2: Early Warning, Instrumentation and Monitoring pp 461–467

CNRBU 146/92 (1992) Determinazione dei moduli di deformazione mediante prova di carico a doppio ciclo con piastra circolare

Coutinho CP, Baptista AJ, Rodrigues JD (2016) Reduced scale models based on similitude theory: A review up to 2015. Eng Struct 119:81–94

Dassault Systèmes (2024) Abaqus 2024 documentation. https://help.3ds.com/2024/English/SIMULIA_AbaqusDoc, accessed: 2024-11-04

Di Prisco C, Vecchiotti M (2003) Impatti di blocchi di roccia su rilevati rinforzati: modellazione teorica e spunti progettuali. L'Ingegnere e l'Architetto 10:62–69

Donzé F (2006) Discrete element group for hazard mitigation. Université Joseph Fourier, Grenoble, Tech. rep

EAD 200086-00-0602 (2019) Guideline for european technical assessment for dowel-type fasteners for timber structures

EN 10223-3 (2013) Steel wire and wire products for fencing and netting - part 3: Hexagonal steel wire mesh products for civil engineering purposes

EN ISO 10319 (2015) Geosynthetics – wide-width tensile test

Ferlisi S, Cascini L, Corominas J et al (2012) Rockfall risk assessment to persons travelling in vehicles along a road: the case study of the amalfi coastal road (southern italy). Nat Hazards 62:691–721

Grimod A, Giacchetti G (2013) Protection from high energy impacts using reinforced soil embankments: Design and experiences. Landslide Science and Practice: Volume 3: Spatial Analysis and Modelling Springer, location: Berlin Heidelberg pp 189–196

Hofmann R, Mölk M (2012) Bemessungsvorschlag für steinschlagschutzdämme. Geotechnik 35(1):22–33

Hofmann R, Vollmert L (2020) Rockfall embankments: construction and design. Geomech Tunn 13(1):21–31

Hofmann R, Vollmert L, Mölk M (2013) Rockfall-protection embankments–design concept and construction details. In: proceedings of 18th International conference on soil mechanics and geotechnical engineering, Paris, France, pp 2–6

Hofmann R, Mölk M, Vollmert L (2017) Steinschlagschutzdämme–bemessungsvorschlag für verschiedene bautypen. geotechnik 40(1):35–53

Jaecklin F (2006) Innovative design for repairing gondo mudslide by 20 m high geogrid wall. In: Proceedings of the 8th international conference on geosynthetics, Ozaka, Japan, pp 1223–1228

Jones N (2011) Structural Impact. Cambridge University Press, Cambridge, UK

Kanno H, Moriguchi S, Hayashi S et al (2021) A computational design optimization method for rockfall protection embankments. Eng Geol 284:105920

Kar AK (1978) Projectile penetration into buried structures. J Struct Div 104(1):125–139

Kister B (2015) Development of basics for dimensioning rock fall protection embankments in experiment and theory (in german), research project fedro 2012/003. FEDRO report 1524

Kister B, Lambert S, Loup B (2017) Impact tests on small scale embankments with rockery-lessons learned. In: Rocexs 2017, pp 4–p

Korini O, Bost M, Rajot JP et al (2021) The influence of geosynthetics design on the behavior of reinforced soil embankments subjected to rockfall impacts. Eng Geol 286:106054

Labiouse V, Descoeudres F, Montani S (1996) Experimental study of rock sheds impacted by rock blocks. Struct Eng Int 6(3):171–176

Lambert S, Bourrier F (2013) Design of rockfall protection embankments: a review. Eng Geol 154:77–88

Lambert S, Kister B (2017) Analysis of existing rockfall embankments of switzerland (aeres). Federal Office for the Environment, Bern, p 55

Lambert S, Kister B (2018a) Efficiency assessment of existing rockfall protection embankments based on an impact strength criterion. Eng Geol 243:1–9

Lambert S, Kister B (2018b) Efficiency assessment of existing rockfall protection embankments based on an impact strength criterion. Eng Geol 243:1–9

Lambert S, Heymann A, Gotteland P et al (2014) Real-scale investigation of the kinematic response of a rockfall protection embankment. Nat Hazard 14(5):1269–1281

Lambert S, Bourrier F, Gotteland P et al (2020) An experimental investigation of the response of slender protective structures to rockfall impacts. Can Geotech J 57(8):1215–1231

Lepert P, Corté J (1988) Centrifuge modeling of the impact of large blocks of rock on a protection structure. In: Proceedings of the International Conference on Geotechnical Centrifuge Modelling: Balkema, location: Rotterdame, pp 457–465

Li Q, Chen X (2003) Dimensionless formulae for penetration depth of concrete target impacted by a non-deformable projectile. Int J Impact Eng 28(1):93–116

Lin YL, Fang PF, Wang X et al (2023) Experimental and numerical study on tensile behavior of double-twisted hexagonal gabion wire mesh. Buildings 13:1657

Lu L, Xiao L, Wang Z et al (2021) Experimental testing of ground reinforced embankments under low-energy impact of rockfall. Rock Mech Rock Eng 54:5667–5681

Marchelli M, De Biagi V, Bertolo D et al (2022) A mixed quantitative approach to evaluate rockfall risk and the maximum allowable traffic on road infrastructure. Georisk Assess Manag Risk Eng Syst Geohazards 16(3):584–594

Marchelli M, Deangeli C et al (2022b) Towards a codified design procedure for rockfall reinforced earth embankments. GEAM, Geoingegneria e attività estrattiva

Mohammadi M, Dai JG, Wu YF et al (2019) Development of extended drucker-prager model for non-uniform frp-confined concrete based on triaxial tests. Constr Build Mater 224:1–18

Mokhtari M, Kalantari B (2019) Behavior of stone columns based on plate load test and fem analysis on the north end of persian gulf. Electron J Geotech Eng 24(5):1317–1326

Mongiovi L, Bighignoli M, Danzi A, et al (2014) An impact test on a reinforced earth embankment. In: Proceedings of Interdisciplinary workshop on rockfall protection–Rocexs

Naeini SA, Taherabadi E (2015) Numerical and theoretical study of plate load test to define coefficient of subgrade reaction. J Geotech Transp Eng 1(2):38–42

Niezrecki C, Reu PL, Baqersad J et al (2020) DIC and Photogrammetry for Structural Dynamic Analysis and High-Speed Testing. Springer, New York, New York, NY, pp 1–70

Officine Maccaferri Italia (2022) Terramesh verde - manuale di installazione (in italian). Tech. rep, Officine Maccaferri Italia Srl

Oggeri C, Ronco C, Vinai R (2021) Validation of numerical dem modelling of geogrid reinforced embankments for rockfall protection. GEAM, Geoingegneria e attività estrattiva

ONR 24810 (2021) Technical protection against rockfall - terms and definitions, effects of actions, design, monitoring and maintenance. Austrian Standards International

Oshiro RE, Alves M (2004) Scaling impacted structures. Arch Appl Mech 74:130–145

Patel A, Ingale R, Bhanarkar KB (2018) Effect of compaction states and the confining pressure on poisson's ratio of stratified and non-stratified soils. Arab J Sci Eng 43:1983–1999

Peila D, Castiglia C, Oggeri C, et al (2000) Full scale tests on geogrid reinforced embankments for rock fall protection. In: Proceedings of the 2nd European Geosynthetics Conference and Exhibition, Bologna, Italy, pp 15–18

Peila D, Oggeri C, Castiglia C, et al (2002) Testing and modelling geogrid reinforced soil embankments to high energy rock impacts. In: Geosynthetics - 7 ICG, pp 133–136

Peila D, Oggeri C, Castiglia C (2007) Ground reinforced embankments for rockfall protection: design and evaluation of full scale tests. Landslides 4:255–265

Peila D et al (2011) Ground reinforced embankments for rockfall protection: From real scale tests to numerical modelling. Rockfall Engineering. John Wiley & Sons, Boca Raton, FL, pp 252–284

Pichler B, Hellmich C, Mang HA (2005) Impact of rocks onto gravel design and evaluation of experiments. Int J Impact Eng 31(5):559–578

Plassiard JP, Donzé FV (2009) Rockfall impact parameters on embankments: a discrete element method analysis. Struct Eng Int 19(3):333–341

Plassiard JP, Donzé FV (2010) Optimizing the design of rockfall embankments with a discrete element method. Eng Struct 32(11):3817–3826

Rajesh S, Viswanadham B (2015) Numerical simulation of geogrid-reinforced soil barriers subjected to differential settlements. Int J Geomech 15(4):04014062

Rimoldi P, Brusa N (2024) Design method for rockfall protection embankments reinforced with geosynthetics. In: Biondi D, altri (eds) Geosynthetics: Leading the Way to a Resilient Planet. CRC Press, Boca Raton, FL, p 1773–1782, open Access: www.taylorfrancis.com, CC BY-NC-ND 4.0 license

Ronco C (2010) I rilevati in terra rinforzata utilizzati per la protezione dei versanti: verifiche numeriche e analitiche di supporto alla progettazione (in italian). PhD thesis, PhD thesis, Politecnico di Torino, Italy

Ronco C, Oggeri C, Peila D (2009) Design of reinforced ground embankments used for rockfall protection. Nat Hazard 9(4):1189–1199

Sestras P, Bilaşco S, Roşca S et al (2022) Multi-instrumental approach to slope failure monitoring in a landslide susceptible newly built-up area: Topo-geodetic survey, uav 3d modelling and ground-penetrating radar. Remote Sensing 14(22):5822

Shehadeh M, Shennawy Y, El-Gamal H (2015) Similitude and scaling of large structural elements: Case study. Alex Eng J 54(2):147–154

Teodoru IB, Toma IO (2009) Numerical analyses of plate loading test. Buletinul Institutului Politehnic din lasi Sectia Constructii Arhitectura 55(1):57

Vigna S, Marchelli M, De Biagi V et al (2023) Numerical simulation of rockfall protection embankments in natural soil. Geosciences 13(12):368

Vigna S, Marchelli M, Colombero C, et al (2024) Rockfall protection embankments: Insights into impact effects. In: New Challenges in Rock Mechanics and Rock Engineering, CRC Press, location: London pp 1465–1470

Volkwein A, Gerber W (2011) Stronger and lighter-evolution of flexible rockfall protection systems. In: IABSE-IASS 2011 London Symposium Report: Taller, Longer, Lighter; IABSE: Zurich, Switzerland

Wang B, Cavers DS (2008) A simplified approach for rockfall ground penetration and impact stress calculations. Landslides 5(3):305–310

Wersäll C, Baker S, Zackrisson P (2023) Stiffness of ballastless railway embankments determined by repetitive static plate load tests. Transportation Infrastructure Geotechnology 10:1032–1049

Wyllie DC (2014) Rock Fall Engineering. CRC Press, Boca Raton, FL

Yong AC, Lam NT, Menegon SJ (2022) Collision Actions on Structures. CRC Press, Boca Raton, FL

Zhao B, Hu J, Chen W et al (2019) Computational method for in-situ finite element modeling of inflatable membrane structures based on geometrical shape measurement using photogrammetry. Comput Struct 224:106105

Zhou WH, Lao JY, Huang Y et al (2016) Three-dimensional finite element modelling of soil arching in pile-supported geogrid-reinforced embankments. Proced Eng 143:607–614

Zou W, Zhang J, Wang X, et al (2012) Influence factors of geogrid–soil interface shear strength and contribution of transverse ribs of geogrid. In: 5th Asian Regional Conference on Geosynthetics, pp 13–15

Publisher's Note Springer Nature remains neutral with regard to jurisdictional claims in published maps and institutional affiliations.